

AD-A220 286

MICROWAVE LABORATORY REPORT NO. 90-P-2

ANALYSIS AND APPLICATIONS OF THE CROSSTIE-OVERLAY SLOW-WAVE
STRUCTURE

TECHNICAL REPORT

YU-DE LIN AND TATSUO ITOH

FEBRUARY 1990

ARMY RESEARCH OFFICE CONTRACT NO. DAAL03-88-K-0005

THE UNIVERSITY OF TEXAS AT AUSTIN
DEPARTMENT OF ELECTRICAL ENGINEERING
AUSTING, TEXAS 78712



APR 09 1990

90 04 09 134

MICROWAVE LABORATORY REPORT NO. 90-P-2

ANALYSIS AND APPLICATIONS OF THE CROSSTIE-OVERLAY SLOW-WAVE
STRUCTURE

TECHNICAL REPORT

YU-DE LIN AND TATSUO ITOH

FEBRUARY 1990

ARMY RESEARCH OFFICE CONTRACT NO. DAAL03-88-K-0005

THE UNIVERSITY OF TEXAS AT AUSTIN
DEPARTMENT OF ELECTRICAL ENGINEERING
AUSTIN, TEXAS 78712

UNCLASSIFIED
SECURITY CLASSIFICATION OF THIS PAGE

MASTER COPY

FOR REPRODUCTION PURPOSES

REPORT DOCUMENTATION PAGE				
1a. REPORT SECURITY CLASSIFICATION Unclassified		1b. RESTRICTIVE MARKINGS		
2a. SECURITY CLASSIFICATION AUTHORITY		3. DISTRIBUTION/AVAILABILITY OF REPORT Approved for public release; distribution unlimited.		
2b. DECLASSIFICATION/DOWNGRADING SCHEDULE		5. MONITORING ORGANIZATION REPORT NUMBER(S) AR0 25045.35-EL		
4. PERFORMING ORGANIZATION REPORT NUMBER(S) Microwave Laboratory Report No. 90-P-2		7a. NAME OF MONITORING ORGANIZATION U. S. Army Research Office		
6a. NAME OF PERFORMING ORGANIZATION The University of Texas		6b. OFFICE SYMBOL (if applicable)		7b. ADDRESS (City, State, and ZIP Code) P. O. Box 12211 Research Triangle Park, NC 27709-2211
6c. ADDRESS (City, State, and ZIP Code) Dept. of Electrical & Computer Engineering The University of Texas Austin, TX 78712		9. PROCUREMENT INSTRUMENT IDENTIFICATION NUMBER DAAC03-88-K-0005		
8a. NAME OF FUNDING/SPONSORING ORGANIZATION U. S. Army Research Office		8b. OFFICE SYMBOL (if applicable)		10. SOURCE OF FUNDING NUMBERS
8c. ADDRESS (City, State, and ZIP Code) P. O. Box 12211 Research Triangle Park, NC 27709-2211		PROGRAM ELEMENT NO	PROJECT NO	TASK NO WORK UNIT ACCESSION NO
11. TITLE (Include Security Classification) Analysis and Applications of the Crosstie-Overlay Slow-Wave Structure				
12. PERSONAL AUTHOR(S) Yu-De Lin and Tatsuo Itoh				
13a. TYPE OF REPORT Technical		13b. TIME COVERED FROM TO		14. DATE OF REPORT (Year, Month, Day)
15. PAGE COUNT				
16. SUPPLEMENTARY NOTATION The view, opinions and/or findings contained in this report are those of the author(s) and should not be construed as an official Department of the Army position, policy, or decision, unless so designated by other documentation.				
17. COSATI CODES			18. SUBJECT TERMS (Continue on reverse if necessary and identify by block number)	
FIELD	GROUP	SUB-GROUP	slow-wave structures, passive circuit elements, distributed filters, frequency-scanning antenna	
19. ABSTRACT (Continue on reverse if necessary and identify by block number) The crosstie-overlay slow-wave structure is proposed as a passive circuit element in monolithic microwave integrated circuits. The propagation characteristics of the crosstie-overlay slow-wave structure are analyzed both analytically and experimentally. In analysis, a method suitable for design as well as a rigorous two-dimensional spectral domain method for accurate results are developed. The results obtained in analysis are checked with experimental results. They are in good agreement. A modified structure is proposed to reduce the conductor loss. Distributed Chebychev bandstop filters utilizing the slow-wave structure are designed. Another circuit application of the slow-wave structure, frequency scanning antenna, is also investigated.				
20. DISTRIBUTION/AVAILABILITY OF ABSTRACT <input checked="" type="checkbox"/> UNCLASSIFIED/UNLIMITED <input type="checkbox"/> SAME AS RPT <input type="checkbox"/> DTIC USERS			21. ABSTRACT SECURITY CLASSIFICATION Unclassified	
22a. NAME OF RESPONSIBLE INDIVIDUAL Tatsuo Itoh			22b. TELEPHONE (Include Area Code) (512) 471-1072	
			22c. OFFICE SYMBOL	

DD FORM 1473, 84 MAR

83 APR edition may be used until exhausted
All other editions are obsolete

SECURITY CLASSIFICATION OF THIS PAGE
UNCLASSIFIED

ANALYSIS AND APPLICATIONS OF THE CROSSTIE-OVERLAY SLOW-WAVE STRUCTURE

Yu-De Lin and Tatsuo Itoh

The crosstie-overlay slow-wave structure is proposed as a passive circuit element in monolithic microwave integrated circuits. The propagation characteristics of the crosstie-overlay slow-wave structure are analyzed both analytically and experimentally. In analysis, a method suitable for design as well as a rigorous two-dimensional spectral domain method for accurate results are developed. The results obtained in analysis are checked with experimental results. They are in good agreement. A modified structure is proposed to reduce the conductor loss. Distributed Chebychev bandstop filters utilizing the slow-wave structure are designed. Another circuit application of the slow-wave structure, frequency scanning antenna, is also investigated.

A-1

TABLE OF CONTENTS

	page
TABLE OF CONTENTS	ii
LIST OF FIGURES	iii
LIST OF TABLES	vi
CHAPTER 1: INTRODUCTION	1
CHAPTER 2: ANALYSIS AND DESIGN	8
CHAPTER 3: A MODIFIED STRUCTURE	31
CHAPTER 4: CIRCUIT APPLICATIONS	44
CHAPTER 5: CONCLUSIONS	65
APPENDIX I: SPECTRAL DOMAIN GREEN'S FUNCTION	66
APPENDIX II: BASIS FUNCTIONS	68
BIBLIOGRAPHY	70

LIST OF FIGURES

	page
Figure 1.1 The crosstie overlay slow-wave structure	3
Figure 1.2 The sideview of the structure	3
Figure 1.3 The cross-sectional view of the structure	4
Figure 1.4 The k_0d - βd diagram of a periodic structure	7
Figure 2.1 The cross-sectional view of the structure with the referenced notations marked for section 2.2	11
Figure 2.2 Relative positions between u-v and x-z coordinates	11
Figure 2.3 The transmission line equivalent circuits for TE-to-y and TM-to y waves	12
Figure 2.4 The cross-sectional view of the structure represented by alternating transmission line sections	16
Figure 2.5 Hypothetical convergence chart of the solutions	22
Figure 2.6 Slow-wave factors versus frequency of a crosstie-overlay structure	24
Figure 2.7 Slow-wave factors versus frequency of a crosstie-overlay structure with thinner dielectric overlay	24
Figure 2.8 Slow-wave factors of section A and section B	28

Figure 2.9	Characteristic impedances of section A and section B	29
Figure 2.10	Slow-wave factors of the crosstie-overlay structure	30
Figure 2.11	The effect of duty cycle on the slow-wave factors of the crosstie-overlay slow-wave structure.	30
Figure 3.1	The recession of metal walls	32
Figure 3.2	The conductor losses of section A and section B	35
Figure 3.3	The modified structure	37
Figure 3.4	Slow-wave factors versus frequency of the modified slow-wave structure	40
Figure 3.5	Slow-wave factors and attenuation constants versus duty cycle of the modified slow-wave structure	42
Figure 3.6	Comparison of the quality factors of the modified and the original crosstie-overlay slow-wave structure	43
Figure 4.1	Distributed Chebychev bandstop filter	45
Figure 4.2	The insertion loss of Chebychev bandstop filters	45
Figure 4.3	The insertion loss and return loss of the bandstop filters	54
Figure 4.4	The anatomical view of the frequency-scanning antenna	57
Figure 4.5	The picture of the antenna picture	58

Figure 4.6	Main beam direction of a leaky-wave antenna	60
Figure 4.7	E-plane radiation pattern for the broadside direction	62
Figure 4.8	The frequency response of the antenna circuit	63

LIST OF TABLES

	page
Table 2.1 Basis functions used in two-dimensional spectral domain approach	21
Table 2.2 Slow-wave factors versus thickness of dielectric	25
Table 3.1 Comparison of the losses of the crosstie-overlay slow-wave structures	40
Table 3.2 Comparison of the slow-wave factors of different structures.	41
Table 4.1 Comparison of the measured and calculated main beam directions versus frequency	64

CHAPTER 1: INTRODUCTION

1.1 Background and Objectives

Due to the rapid development of GaAs technology, monolithic microwave integrated circuits (MMIC's) have been receiving considerable attention recently [1]. The low-loss property of semi-insulating GaAs substrate and the excellent microwave performance of metal-semiconductor field-effect-transistors (MESFET's) make a truly monolithic microwave integrated circuit feasible for the first time. One of the main requirements of MMIC's is the miniaturization of passive circuit elements. Conventional transmission lines can only support waves with the smallest possible wavelength equal to $\lambda_0/\sqrt{\epsilon_r}$, with λ_0 being the free space wavelength and ϵ_r the dielectric constant of the substrate of the transmission lines. For this reason, slow-wave structures, which support wave propagation with smaller wavelengths than conventional transmission lines, are very suitable as the transmission structures in MMIC's.

There are several slow-wave structures proposed to date. One of them is the metal-insulator-semiconductor (MIS) slow-wave structure [2], which employs the lossy semiconductor layer to produce the slow-wave propagation. The Schockty-contact structure [3], [4], a variation of the MIS slow-wave structure, uses the same slow-wave mechanism but in which the wave velocity can be varied via DC bias. Another tunable structure is the optically-illuminated coplanar waveguide [5], [6], which uses optically induced electron-hole plasma in the lossy layer to introduce the slow-wave propagation.

The aforementioned structures have the drawback of being inherently lossy due to the fact that it employs the lossy dielectric to create slow-wave mechanism. Recently, the crosstie-overlay slow-wave structure, which is a modification of the structure in [7] for easier fabrication, has been proposed in [8]. Instead of using the lossy dielectric, the crosstie-overlay slow-wave structure uses the periodic structure to create the slow-wave mechanism. Fig. 1.1 shows the perspective view of the structure. In this structure, the periodic crosstie conductors create the slow-wave effect by separating the electrical and magnetic energy propagating in the structure.

The objectives of this study are to analyze the slow-wave propagation in the crosstie-overlay slow-wave structure and to obtain the design data of this structure. After the characterizations of the structure are performed, these data will be applied to circuit design.

1.2 Features of the Crosstie Overlay Slow-Wave Structure

The dielectric overlay between two conductors has been utilized in the MMIC to create high capacitance in [9]. In the crosstie-overlay slow-wave structure, this high-capacitance sections are periodically inserted into common transmission-lines to create the slow-wave effect. The perspective view of the crosstie overlay slow-wave structure is shown in Fig. 1.1. On top of the conventional coplanar waveguide transmission line, a thin dielectric overlay is deposited, and then periodic conductors are evaporated. The crosstie conductors make the structure a periodic structure in the propagation direction (z -direction in Fig. 1.1). The side view and the cross-sectional view are shown in Fig. 1.2 and Fig. 1.3 respectively. From the side view in Fig. 1.2, we can see that each period consists of two sections: (1) the one with crosstie conductor,

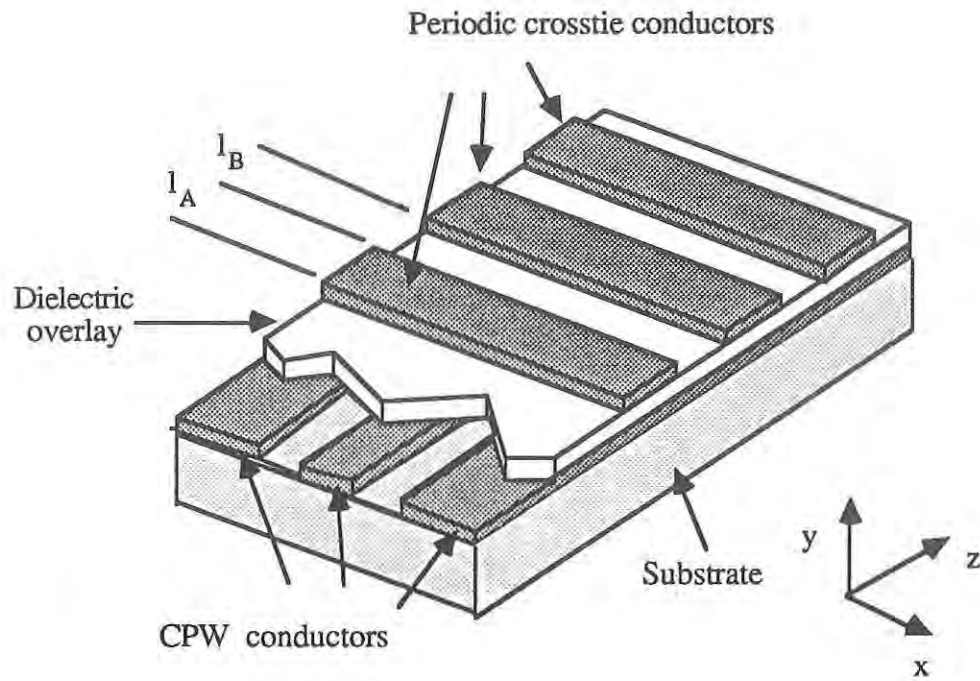


Fig. 1.1 The Crosstie Overlay Slow-Wave Structure.

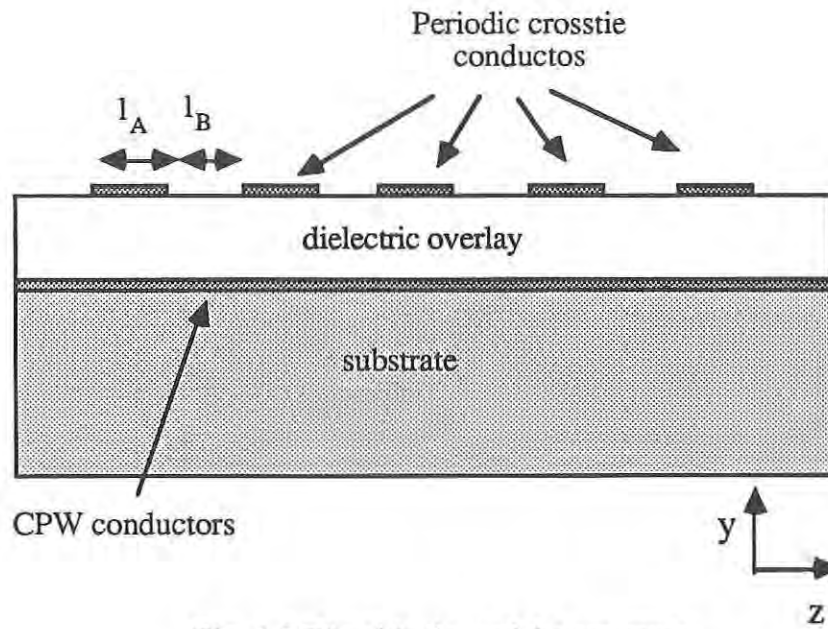


Fig. 1.2 The sideview of the structure.

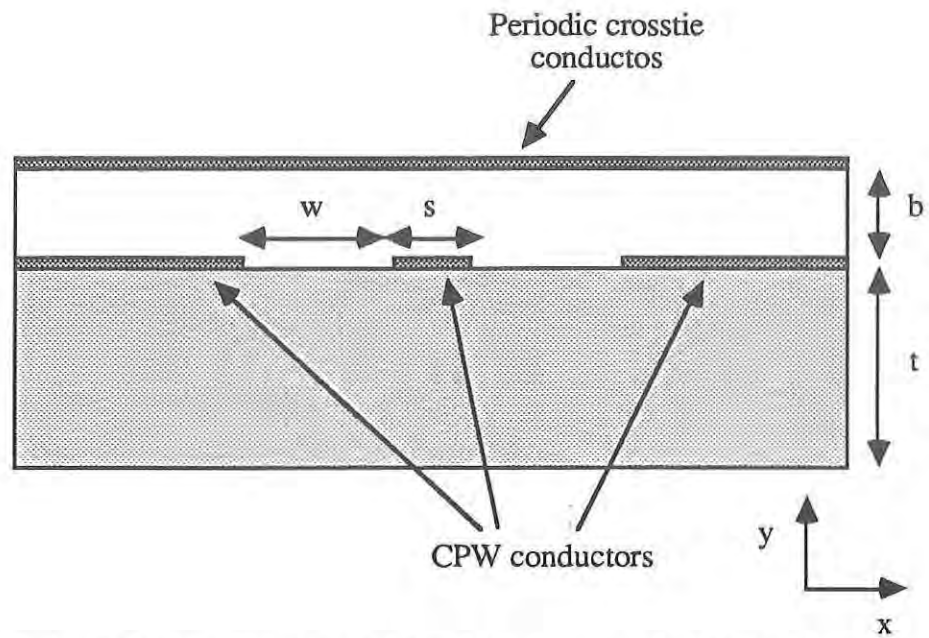


Fig. 1.3(a) The cross-sectional view of th structure for section A.

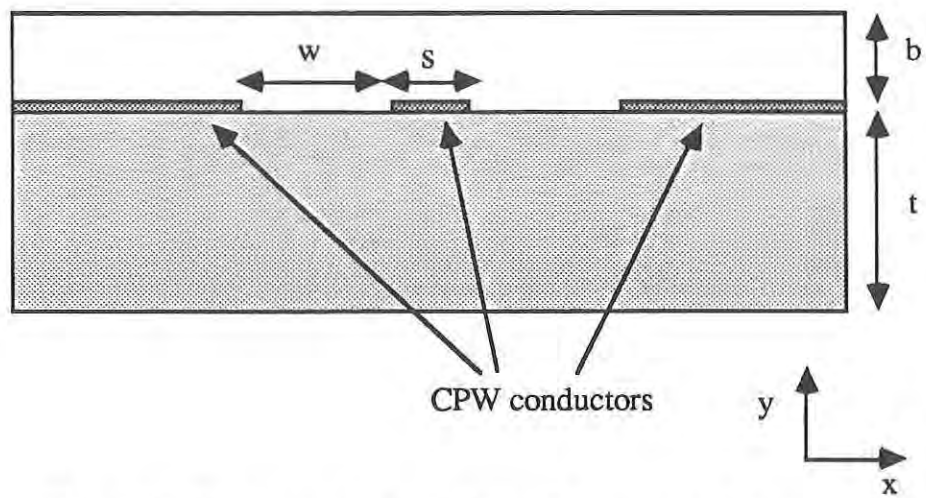


Fig. 1.3(b) The cross-sectional view of th structure for section B.

denoted as section A, and its cross-sectional view is shown in Fig. 1.3(a), and (2) the one without crosstie conductor, denoted as section B and its cross-sectional view is shown in Fig. 1.3(b).

The slow-wave mechanism in the crosstie overlay slow-wave structure is created by the separation of the electric and magnetic energy: the electric energy is concentrated under section A's (low-impedance sections), while the magnetic energy under section B's (high-impedance sections).

1.3 Periodic Structures and Floquet's Theorem

As stated above, the crosstie overlay slow-wave structure is a periodic structure. For better understanding and analysis of the structure, the general properties of periodic structures will be elaborated in this section.

The basic theorem underlying the analysis of periodic structures is Floquet's theorem[10], which states that the fields propagating in a periodic structure are periodic function times a propagation factor, or expressed as:

$$\Phi(x, y, z+d) = \Phi(x, y, z) e^{-j\beta d} \quad (1.1)$$

where β is the propagation constant and d is the length of a period.

From Floquet's theorem, we can expand the fields into Fourier series as:

$$\Phi(x, y, z) = \sum_n \widehat{\Phi}_n(x, y) e^{j(\beta + \frac{2n\pi}{d})z} = \sum_n \widehat{\Phi}_n(x, y) e^{j\beta_n z} \quad (1.2)$$

these β_n 's are usually called spatial harmonics.

The k - β diagram of a typical periodic structure is shown in Fig. 1.4. When kd is small compared to π (d is small compared to the guided wavelength), as indicated on the diagram with an arrow, the kd - βd line is almost a straight line, which means it is dispersionless in this frequency range. Therefore, if the structure is used as transmission line, the operating frequencies should be chosen around this range. When $\beta d = \pi$, or point A marked on the diagram, the first stopband appears. For bandstop filter applications, the stopband center frequency is at this point. When $\beta d = 2\pi$, or point B on the diagram, the second stopband appears, which supports fast wave by the -1th spatial harmonic. Therefore, for antenna applications, the operating frequency should be chosen around this point.

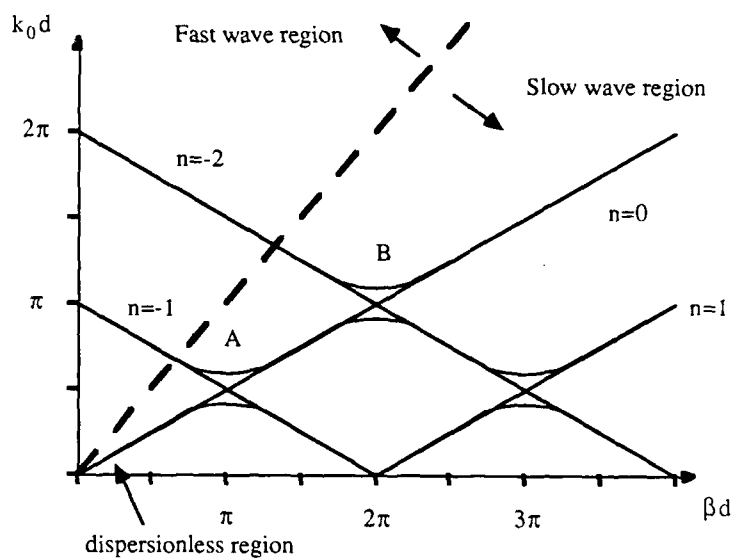


Fig. 1.4. The $k_0 d$ - βd diagram of a periodic structure.

CHAPTER 2: ANALYSIS AND DESIGN

2.1 Introduction

After the properties of the crosstie-overlay slow-wave structure are elaborated in chapter 1, these properties will be utilized in this chapter to develop the methods of analysis, and then these methods will be used to obtain the design data for this structure.

As mentioned in chapter 1, the crosstie-overlay slow-wave structure is a periodic structure. Therefore, Floquet's theorem will be incorporated into the spectral domain approach (SDA) to analyze the propagation characteristics of this structure. Depending on when Floquet's theorem is applied in the procedure of analysis, two methods of analysis are developed: (1) the two-dimensional spectral domain approach, which will be elaborated in section 2.2, and (2) the cascaded transmission line method, which will be discussed in section 2.3.

The first method is to extend the conventional SDA into a two-dimensional method based on Floquet's theorem. This method takes into account the effects of the discontinuities between junctions of the uniform transmission lines. The second method is to treat the crosstie-overlay slow-wave structure as a periodic cascaded transmission lines. The conventional SDA is used first to obtain the propagation characteristics of each transmission line and then Floquet's theorem is applied to the transmission coefficient matrix to obtain the propagation characteristics of the whole structure. The first method has the advantage of being more precise in describing the real physical situation, yet on the expense of extensive numerical efforts. Although

the second method neglects the discontinuities, it is shown to be reasonably accurate and lends more insight into the design consideration.

2.2 The Two-Dimensional Spectral Domain Approach

The spectral domain approach (SDA) has been proven to be effective and efficient in characterization of planar transmission lines in the past two decades [11],[12]. Compared to other methods of analysis for planar transmission lines, the SDA has the advantages of simple formulation and less numerical expense, besides the fact that it is a full-wave analysis and can predict the dispersion behaviors correctly.

In the SDA, the Fourier transform is applied to suppress one of the spatial dependence (x-direction in Fig. 1.1) and the partial differential equations are transformed into ordinary differential equations. Then, the boundary conditions are matched in the transform domain (spectral domain) to obtain the spectral domain Green's functions. Since the differential operators are replaced by multiplication factors, only algebraic equations are handled, which makes the derivation of the spectral domain Green's function very easy.

From Floquet's theorem, the fields propagating in the crosstie-overlay slow-wave structure can be expanded into Fourier series in the propagation direction (z-direction in Fig. 1.1). Therefore, it is straightforward to expand the SDA into a two-dimensional method to analyze the propagation characteristics of the crosstie-overlay slow-wave structures.

The following derivation is based on the immittance approach of the SDA developed in [13]. In the immittance approach, the transmission-line analogy of wave impedance is employed and the matching of the boundary conditions is performed by solving the transmission-line equations. This approach lends more physical insight of the problem and alleviates the tedious and error-prone formulations, especially in the case of complicated structures, such as multi-conductor or multi-layer structures.

Referring to Fig. 1.1, the structure is divided into four homogeneous regions: in y-direction in Fig. 2.1, except conductors between regions, which are assumed to be infinitesimally thin. From Floquet's theorem, all fields in the four regions can be expressed as:

$$E_y(x,y,z) = \sum_{n=-\infty}^{\infty} \int_{-\infty}^{\infty} \widehat{E}_y(\alpha, \beta_n, \beta, y) e^{j(\alpha x + \beta z + \beta_n z)} d\alpha \quad (2.1)$$

where β is the propagation constant, α is the x-direction Fourier transform variable, and β_n is the z-direction Fourier series variable (spatial harmonic).

From this, we recognize that all the fields are a supersposition of inhomogeneous waves propagating in the direction of θ from the direction of z axis where

$$\theta = \cos^{-1} \left(\frac{\beta + \beta_n}{\sqrt{\alpha^2 + (\beta + \beta_n)^2}} \right) \quad (2.2)$$

For each θ (each spectral component), the fields can be decomposed into TE-to-y and TM-to-y waves. In the u-v coordinates defined in Fig. 2.2, the TE-to-y

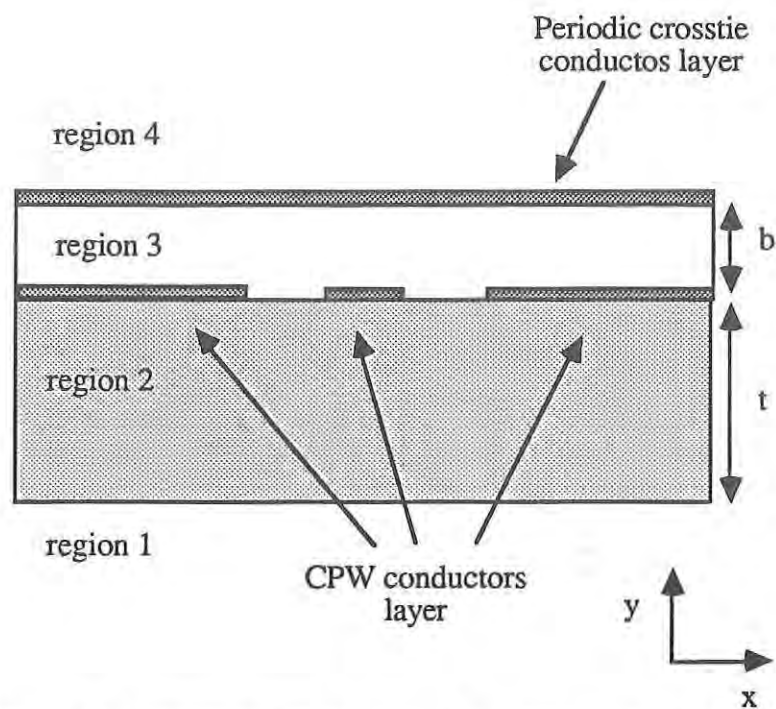


Fig. 2.1 The cross-sectional view of the crossie-overlay structure with the referenced notations marked for Sec. 2.2.

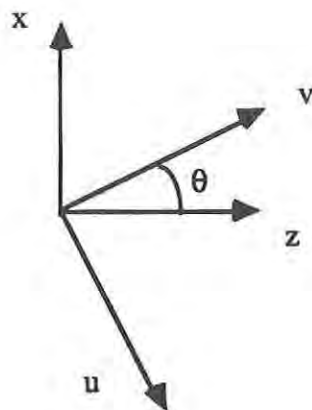


Fig. 2.2 Related positions between u - v and x - z coordinates.

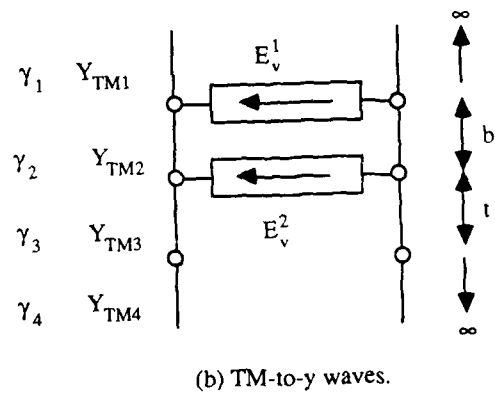
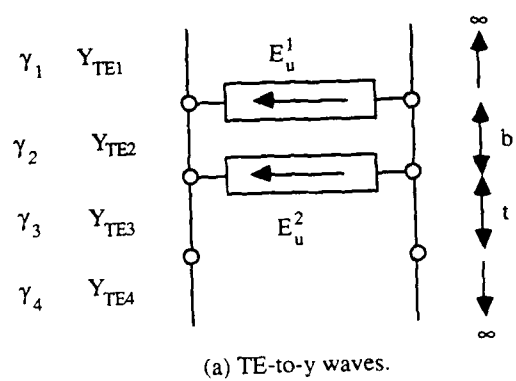


Fig. 2.3 The transmission-line equivalent circuits.

waves contains (E_y , E_u , H_v) fields only and the TM-to-y waves contains (H_y , H_u , E_v) only. Hence, the TE-to-y and TM-to-y waves can be represented by the equivalent circuits shown in Fig. 2.3 with the wave impedance of each region defined as:

$$Y_{TMi} = \frac{j\omega\epsilon_0\epsilon_i}{\gamma_i} \quad (2.3)$$

$$Y_{TEi} = \frac{\gamma_i}{j\omega\mu} \quad (2.4)$$

where $i=1, 2, 3, 4$ denotes the regions shown in Fig. 2.1 and

$$\gamma_i = \sqrt{\alpha^2 + (\beta + \beta_n)^2 - \epsilon_i k^2} \quad (2.5)$$

And the coordinate transformations between u-v and x-z are:

$$u = z \sin\theta - x \cos\theta \quad (2.6)$$

$$v = z \cos\theta + x \sin\theta \quad (2.7)$$

In Fig. 2.3, E^1 's denotes the electric fields on the cross-tie conductors plane and E^2 's, the fields on the coplanar waveguide plane. All the boundary conditions are incorporated into the equivalent circuits. For instance, the air regions (region 1 and region 4) are represented by matched loads. After matching the boundary conditions and mapping the spectral domain admittance matrix in the x-z coordinates, the spectral domain Green's function looks like:

$$\begin{bmatrix} \hat{Y}_{XX}^{11} & \hat{Y}_{XZ}^{11} & \hat{Y}_{XX}^{12} & \hat{Y}_{XZ}^{12} \\ \hat{Y}_{ZX}^{11} & \hat{Y}_{ZZ}^{11} & \hat{Y}_{ZX}^{12} & \hat{Y}_{ZZ}^{12} \\ \hat{Y}_{XX}^{21} & \hat{Y}_{XZ}^{21} & \hat{Y}_{XX}^{22} & \hat{Y}_{XZ}^{22} \\ \hat{Y}_{ZX}^{21} & \hat{Y}_{ZZ}^{21} & \hat{Y}_{ZX}^{22} & \hat{Y}_{ZZ}^{22} \end{bmatrix} \begin{bmatrix} \hat{E}_X^1 \\ \hat{E}_Z^1 \\ \hat{E}_X^2 \\ \hat{E}_Z^2 \end{bmatrix} = \begin{bmatrix} \hat{J}_X^1 \\ \hat{J}_Z^1 \\ \hat{J}_X^2 \\ \hat{J}_Z^2 \end{bmatrix} \quad (2.8)$$

The details of the spectral domain admittance matrix are formulated in appendix I.

To obtain the propagation characteristics of the structure, Galerkin's testing method is applied on Eq. (2.8). First, the unknown electric fields at the conductor layers, E_x^1 's, are expanded into known basis functions with unknown coefficients in the following fashion:

$$E_x^1(x, z) = \sum_{m,l} c_{ml} f_m^1(x) g_l^1(z) \quad (2.9)$$

And the Fourier transform of these are substituted into Eq. (2.8) as:

$$\hat{E}_x^1(\alpha, \beta) = \sum_{m,l} c_{ml} f_m^1(\alpha) g_l^1(\beta) \quad (2.10)$$

The chosen basis functions will be elaborated in the section 2.4 and appendix II. Galerkin's method is then applied by using each basis function as a testing function. Both sides of Eq.(2.8) are multiplied with each basis function and integrated throughout the spectral domain. The right-hand side terms of the equations after the testing procedure will be equal to zero due to Parseval's theorem.

Therefore, after the Galerkin's method is applied, the characteristic equations look like:

$$[A_{m|mT}^{ij}][c_{mI}^{ij}] = 0 \quad (2.11)$$

where the element of the matrix is as

$$A_{mI}^{11} = \sum_{n=-\infty}^{\infty} \int_{-\infty}^{\infty} f_m^1 f_m^{*1} \widehat{Y_{xx}^{11}}(\alpha, \beta_n, \beta, y) g_I^1 g_I^{*1} d\alpha \quad (2.12)$$

The propagation constant is obtained by setting the determinant of the above matrix equal to zero.

2.3 The Cascaded Transmission Lines

From the sideview of the crosstie-overlay slow-wave structure as shown in Fig. 1.2, we can represent the crosstie overlay slow-wave structure as periodic cascaded transmission lines with each period consisting of two sections: (1) section A, the one with crosstie conductors on top of dielectric overlay, of which the cross-sectional view is shown in Fig. 1.3(a), and (2) section B, the one without crosstie conductors on top of the dielectric overlay, of which the cross-sectional view is shown in Fig. 1.3(b). Therefore, the structure can be represented by the periodic cascaded transmission lines equivalent circuit as shown in Fig. 2.4.

In this approach, the conventional SDA is performed to obtain the propagation constants and characteristic impedances of section A and section B respectively. The analysis procedure is as outlined in section 2.2 except that only the x-direction Fourier transform is applied. After these propagation characteristics of these constituent sections are attained, Floquet's theorem is applied to the transmission matrix of the cascaded transmission lines in Fig. 2.4. In this figure, the length,

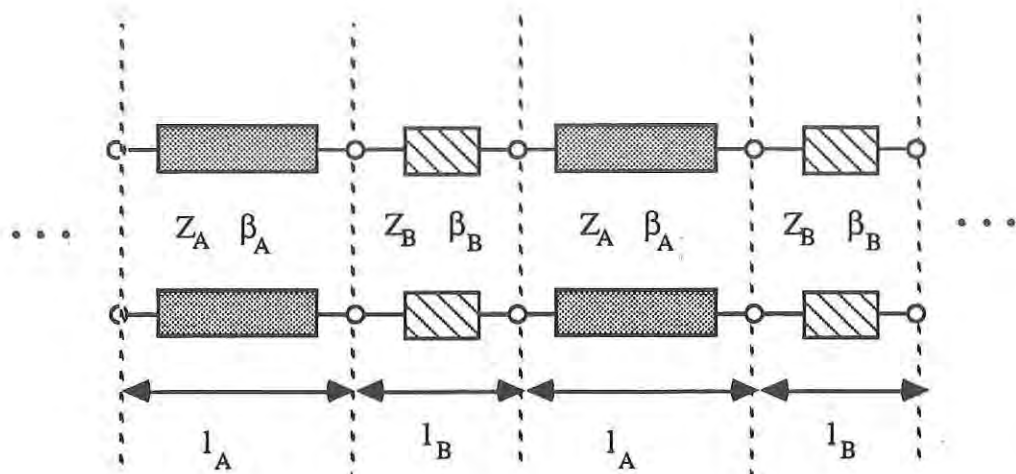


Fig. 2.4. The crosstie overlay slow-wave structure represented by alternating transmission line sections.

propagation constant, and characteristic impedance of section A are denoted as l_A , γ_A , and Z_A respectively, and those of section B, l_B , γ_B , and Z_B . The length of a period d is equal to $l_A + l_B$. From Floquet's theorem, the voltage and current wave one period apart should be equal to each other except a propagation phase delay, or:

$$V_{n+1} = e^{-\gamma d} V_n \quad (2.13)$$

$$I_{n+1} = e^{-\gamma d} I_n \quad (2.14)$$

where γ is the propagation constant of the periodic structure.

If these equations are written in the transmission matrix form, they look like:

$$\begin{bmatrix} V_n \\ I_n \end{bmatrix} = \begin{bmatrix} e^{\gamma d} & 0 \\ 0 & e^{\gamma d} \end{bmatrix} \begin{bmatrix} V_{n+1} \\ I_{n+1} \end{bmatrix} = \begin{bmatrix} A_{\text{unit}} & B_{\text{unit}} \\ C_{\text{unit}} & D_{\text{unit}} \end{bmatrix} \begin{bmatrix} V_{n+1} \\ I_{n+1} \end{bmatrix} \quad (2.15)$$

where the unit transmission matrix of one period is obtained by multiplication of the transmission matrices of section A and section B:

$$\begin{aligned} \begin{bmatrix} A_{\text{unit}} & B_{\text{unit}} \\ C_{\text{unit}} & D_{\text{unit}} \end{bmatrix} &= \begin{bmatrix} A_A & B_A \\ C_A & D_A \end{bmatrix} \begin{bmatrix} A_B & B_B \\ C_B & D_B \end{bmatrix} \\ &= \begin{bmatrix} \cosh(\gamma_A l_A) & Z_A \sinh(\gamma_A l_A) \\ Y_A \sinh(\gamma_A l_A) & \cosh(\gamma_A l_A) \end{bmatrix} \begin{bmatrix} \cosh(\gamma_B l_B) & Z_B \sinh(\gamma_B l_B) \\ Y_B \sinh(\gamma_B l_B) & \cosh(\gamma_B l_B) \end{bmatrix} \end{aligned} \quad (2.16)$$

Solving Eq. (2.15) and (2.16), the propagation constant of the periodic structure, γ , can be obtained from the dispersion equation of the periodic structure:

$$\cosh(\gamma d) = \cosh(\gamma_A l_A) \cosh(\gamma_B l_B) + \frac{1}{2} \left(\frac{Z_A}{Z_B} + \frac{Z_B}{Z_A} \right) \sinh(\gamma_A l_A) \sinh(\gamma_B l_B) \quad (2.17)$$

Assume the lossless case is under consideration, or $\gamma=j\beta$, then Eq. (2.17) becomes:

$$\cos(\beta d) = \cos(\beta_A l_A) \cos(\beta_B l_B) - \frac{1}{2} \left(\frac{Z_A}{Z_B} + \frac{Z_B}{Z_A} \right) \sin(\beta_A l_A) \sin(\beta_B l_B) \quad (2.18)$$

The characteristic impedance of the periodic structure at the end of a unit cell can be obtained in similar fashion by solving Eq. (2.15) and (2.16):

$$Z_p^\pm = \frac{2B_{\text{unit}}}{D_{\text{unit}} - A_{\text{unit}} \pm \sqrt{(A_{\text{unit}} + D_{\text{unit}})^2 - 4}} \quad (2.19)$$

where the signs represent the direction of the propagation.

2.3.2 Design Equations

For circuit design, it is necessary to relate the propagation characteristics to the size of the circuit directly. From the dispersion relationship of the crosstie-overlay slow-wave structure, Eq. (2.18), assuming that the length of each constituting section is small compared to the guided wavelength and the impedance ratio between the two constituent sections is very large, which are the operating conditions desired, we arrive at:

$$\beta = \frac{\frac{Z_B}{Z_A} \beta_A \beta_B l_A l_B}{(l_A + l_B)^2} \quad (2.20)$$

Finding the extremum for Eq. (2.20) by differentiating β with respect to l_A and l_B , respectively, the maximum slow-wave factor that can be achieved is when $l_A=l_B$, and the propagation constant under this condition is:

$$\beta = \frac{\sqrt{\frac{Z_B}{Z_A}}}{2} \sqrt{\beta_A \beta_B} \quad (2.21)$$

From this equation, we can also estimate the impedance ratio required for a designated slow-wave factor. This equation combined with the design data charts of the propagation constants and characteristic impedances of section A and section B, the physical sizes of required circuit can be obtained.

2.4 Numerical Considerations

In order to obtain numerical stability and save numerical expenses, some measures should be taken when performing the SDA. Appropriate considerations of the physical conditions required and discreet implementations of these conditions into the computer program not only guarantee the correctness of the numerical solutions but also expedite their convergence. Also, some numerical schemes are necessary to save the execution time and computer memory.

2.4.1 Choice of the basis functions

The choice of the basis functions for the conductor layers is very important in the SDA in that it influences the convergence and correctness of the solutions. These basis functions should comply with the following physical and mathematical conditions [14], [15]:

- (1) They should satisfy the edge conditions at the edge of the conductor strip.
- (2) These basis functions should form a complete set of bases and their Fourier transform analytically obtainable.
- (3) To avoid the spurious modes, the basis functions should be twice differentiable.

With the above conditions in mind, the following are suitable basis functions :

- 1. Maxwell functions
- 2. Legendre functions
- 3. Localized triangular functions.

The definitions of these basis functions are explained in Appendix II.

In the 2-D SDA, the basis functions used are listed in Table 3.1. In the 1-D SDA of the cascaded transmission line method, the Maxwell functions are used.

2.4.2 Convergence Considerations

All numerical methods should be performed in consideration of the finiteness of the computer resources, and the spectral domain approach is no exception. Specific properties of the problem such as the symmetry of the characteristic equation matrix, the reusable basis functions during iterations are taken into account in the programming to save computation time and assure fast convergence of the solutions.

	x-direction	z-direction
$E_x^1 \ E_z^1$	Localized triangular functions	Maxwell functions
$E_x^2 \ E_z^2$	Maxwell functions	Localized triangular functions

Table 2.1 Basis functions used in the two-dimensional SDA.

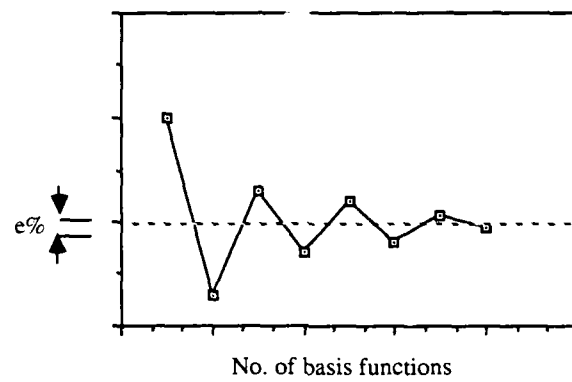


Fig. 2.5 Hypothetical convergence chart of the solutions.

Another concern is the number of basis functions required to obtain a convergent solution. A hypothetical convergence chart of the solution versus number of basis functions is shown in Fig. 2.5. The number of the basis functions is increased until the solutions are within certain range of error.

2.5 Numerical Results

2.5.1 Preliminary Results

The slow-wave factor, β/k_0 , or the propagation constant normalized by the free space wave number, measures the effectiveness of the slow-wave structures. The numerical results obtained by both methods discussed in previous sections are presented, and they are compared with experimental results whenever available. The convergence check mentioned in section 2.4 is performed to determine the convergence of the numerical results. The measurement of the slow-wave factors is performed on an HP 8510 vector network analyzer by the phase delay method.

The slow-wave factors for one set of circuit parameters, obtained both by analysis method and experiments, are shown in Fig. 2.6. The stopband phenomenon of the cross-tie-overlay slow-wave structure is demonstrated. The measured and calculated data are in good agreement.

The slow-wave factors for another set of parameters of the circuit with thinner dielectric are also presented in Fig. 2.7. Numerical data obtained by both methods are again in good agreement with the measured data.

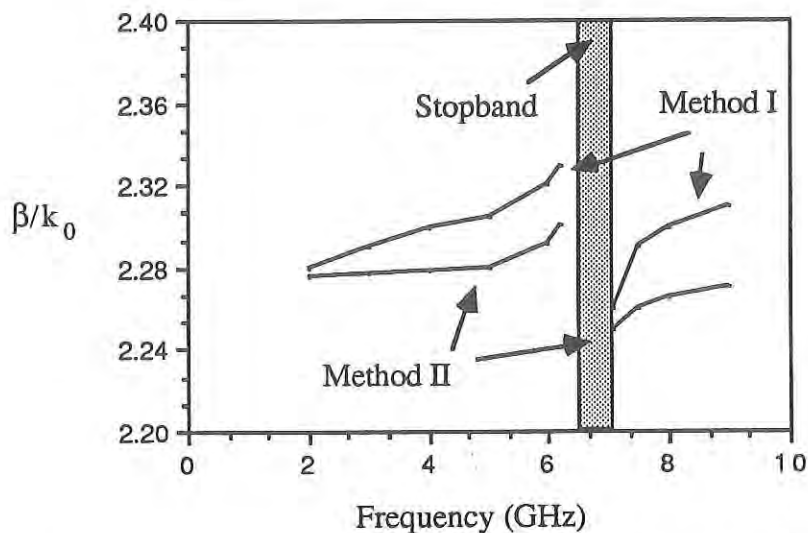


Fig.2.6. The slow-wave factors versus frequency. Dielectric constant of dielectric: 2.55. Dielectric constant of substrate: 10.2. $b = 0.813$ mm. $t = 0.635$ mm. $l_A = 5$ mm. $l_B = 5$ mm. Measured stopband: 6.3-7.1 GHz. Calculated stopband: Method I, 6.4-7.0 GHz; Method II 6.4-6.8 GHz.

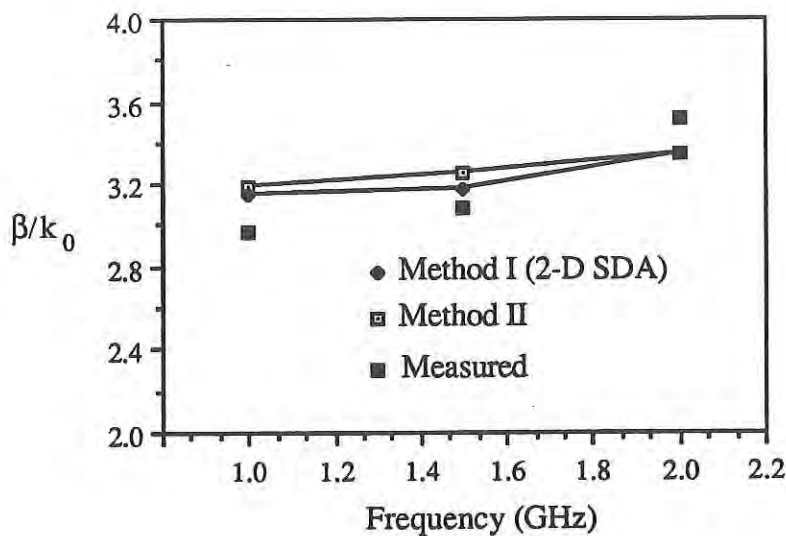


Fig. 2.7 Slow-wave factors versus frequency for thinner dielectric overlay. Dielectric constant of dielectric overlay: 2.1. Dielectric constant of substrate: 10.2. $b = 0.0254$ mm. $t = 0.635$ mm. $s = 1.2$ mm. $w = 0.355$ mm. $l_A = 5$ mm. $l_B = 5$ mm.

b (mm)	Method I	Method II
0.813	2.25	2.28
0.1	2.40	2.38
0.05	2.82	2.85
0.01	5.21	4.76

Table 2.2 The slow-wave factors versus thickness of dielectric overlay. $f = 1\text{GHz}$. All the other parameters are as those of Fig. 2.6.

The slow-wave factors versus thickness of the dielectric overlay are shown in Table 2.2. As shown in Table 2.2, when the thickness of the dielectric decreases, the slow-wave factor increases. This is expected since the coupling between the conductor layers becomes stronger when the thickness of the dielectric becomes thinner. Or this can be explained from the cascaded transmission lines model: we can see that the impedances of the low impedance sections becomes lower when the thickness of dielectric decreases. Therefore, from the discussion in section 2.3.2, the slow-wave factor should increase.

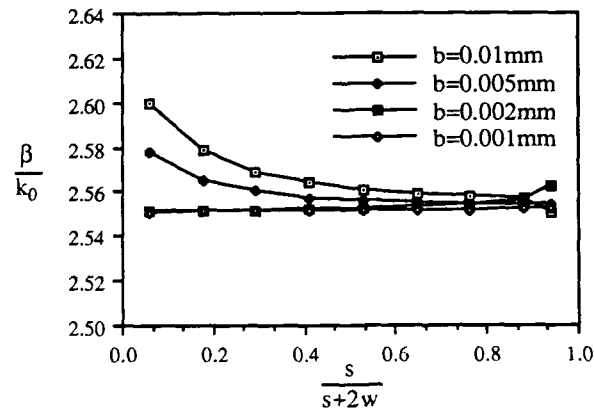
As shown in the above discussions, the numerical results obtained by both methods are within the measurement error of the experimental equipment. Method I, the two-dimensional spectral domain approach, requires much more numerical effort. Besides, method II, the cascaded transmission lines method, is more suitable for the design data characterization due to the fact that it can relate the circuit size to propagation characteristics more directly. Therefore, this method is used to obtain the design data chart presented in the following sections

2.5.2 Design Data Charts

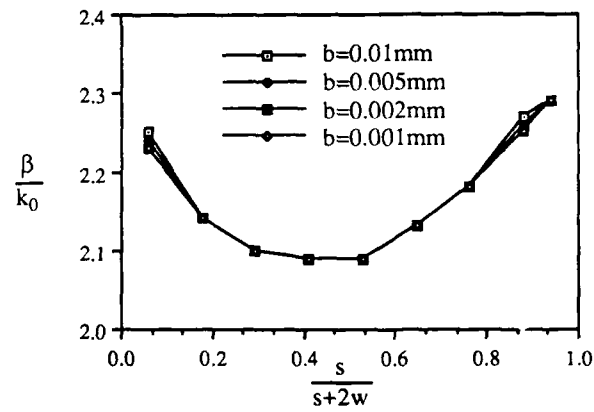
For the convenience of circuit design and to understand the properties of the cross-tie-overlay slow-wave structures, the propagation properties of the constituent sections (section A and section B) and the structure are characterized with several circuit parameters in this section. The examples shown below use the semi-insulating GaAs ($\epsilon_r=12.9$) as substrate and Si_3N_4 ($\epsilon_r=6.5$) as dielectric overlay, which are the most commonly used materials in MMIC. The other circuit parameters are noted in the figures.

Fig. 2.8 shows the variations of the slow-wave factors of section A and section B with respect to the thickness of the dielectric overlay and the coplanar waveguide aspect ratio, $s/(s+2w)$. As shown in these figures, the thickness of the dielectric overlay does not affect the propagation constant of section A and section B. The aspect ratio affects the propagation constants of section B more than those of section A. Fig. 2.9 shows the variations of the characteristic impedances of section A and section B with respect to the thickness of the dielectric overlay and the aspect ratio. The impedances of section A and section B are very different as shown. The high impedance ratio makes the slow-wave propagation possible. The impedances of both sections decrease with larger aspect ratio. Also, the thickness of the dielectric overlay affects more the impedance of section A. The impedance variation of section A with respect to the aspect ratio covers a wide range, which is very useful in circuit design. These data charts combined with the design equations in 2.3.2 can determine the physical parameters of the circuit desired.

Fig. 2.10 shows the slow-wave factors of the crosstie-overlay slow-wave structure with different dielectric overlay thicknesses and aspect ratio. The slow-wave factors increase as the thickness of the dielectric overlay decreases, as explained in sec 2.3. Fig. 2.11 shows the effect of the duty cycle, l_A/l_A+l_B , on the slow-wave factors of the structure. As expected, when $l_A=l_B$, the slow-wave factor is at maximum.

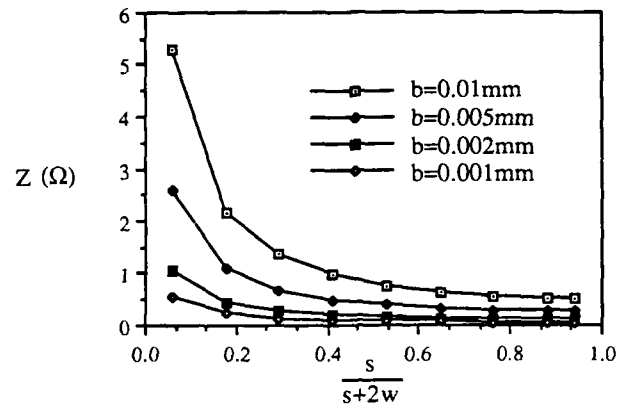


(a)

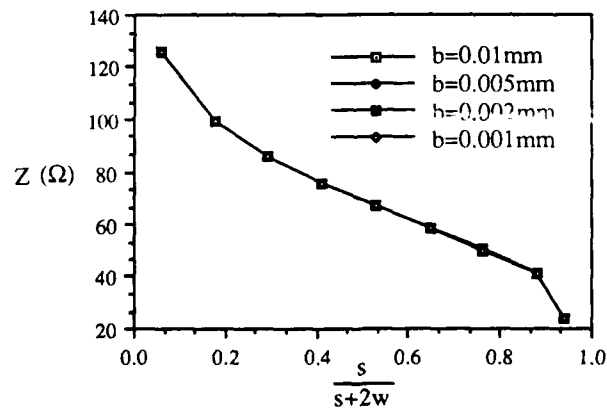


(b)

Fig. 2.8. The slow-wave factors of (a) section A and (b) section B. Dielectric constant of dielectric: 6.5. Dielectric constant of substrate: 12.9. $s+2w=3.4\text{mm}$. $t = 0.508\text{ mm}$. $f=10\text{GHz}$. b is varied as shown



(a)



(b)

Fig. 2.9 The impedances of (a) section A and (b) section B. The physical parameters are as those of Fig. 2.8.

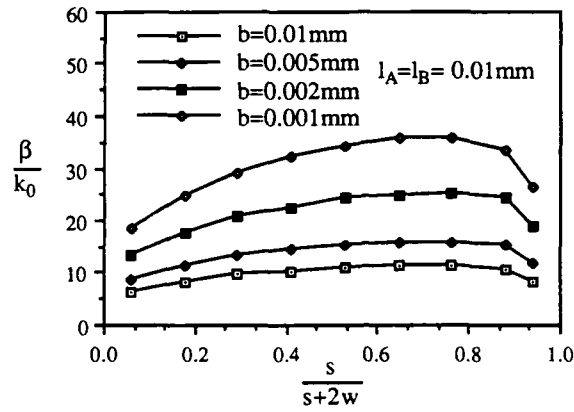


Fig. 2.10 The slow-wave factors of the crosstie-overlay slow-wave structures. The other physical parameters are as those of Fig. 2.8, unless specified.

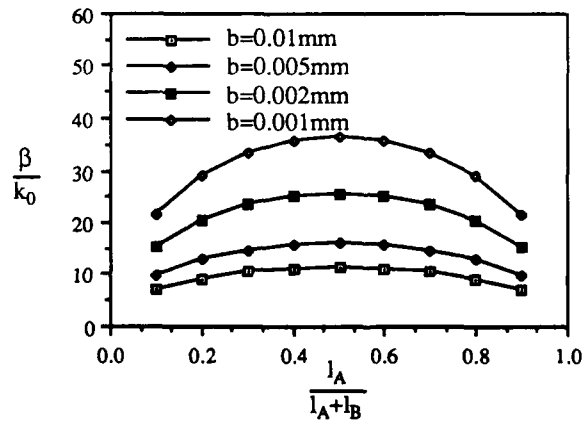


Fig. 2.11 The effect of the duty cycle on the slow-wave factors of the crosstie-overlay slow-wave structure. The physical parameters are as those of Fig. 2.8, unless specified.

CHAPTER 3: A MODIFIED STRUCTURE

3.1 Considerations of Conductor Loss

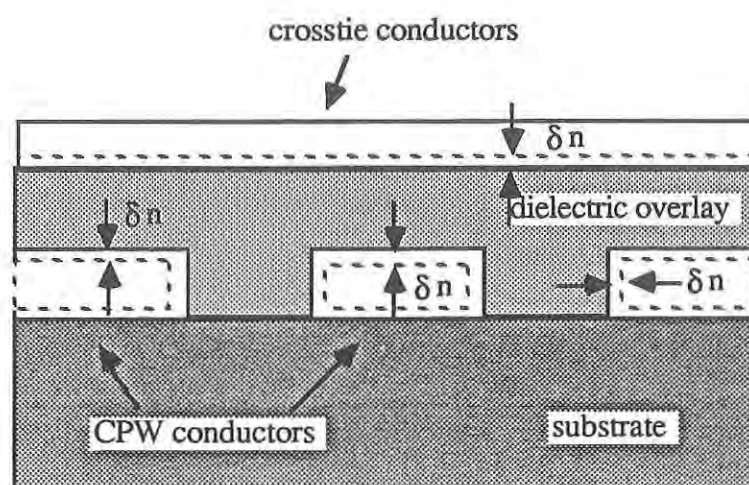
As seen in chapter 2, the slow-wave effect of the crosstie-overlay slow-wave structure increases as the thickness of the dielectric overlay decreases due to the fact that the coupling between the two conductor layers becomes stronger. Therefore, in order to achieve better slow-wave propagation, the thickness of the dielectric should be as thin as possible. Yet, an examination of the conductor loss reveals that the conductor loss of this structure also increases with the decrease of the thickness of the dielectric overlay. In this section, a method of estimation of the conductor loss will be presented. After the behavior of the conductor loss is studied, the crosstie overlay structure is modified to reduce the conductor loss.

The following method is based on the incremental inductance rule in [16]. For a conductor, the surface impedance, $Z_s (=R_s+jX_s)$, has equal real and imaginary parts, that is

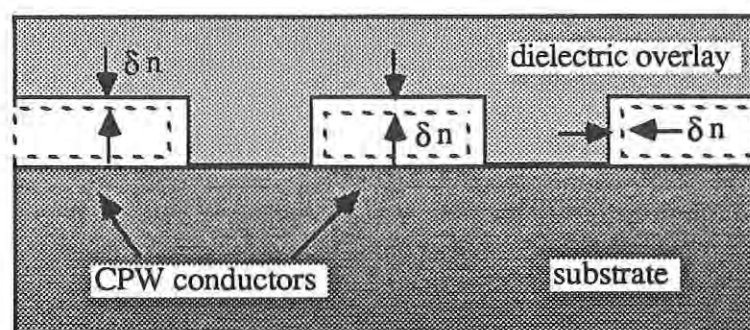
$$R_s=X_s=\omega L_i \quad (3.1)$$

The incremental inductance, L_i , is obtained by the increase of the external inductance, L , due to the recession of the metal walls. This situation is shown in Fig. 3.1. The amount of recession is equal to half of the skin depth, δ . Therefore, according to [16], that is

$$L_i = \sum_m \frac{\mu_m}{\mu_0} \frac{\partial L}{\partial n_m} \frac{\delta_m}{2} \quad (3.2)$$



(a)



(b)

Fig. 3.1 The recession of the metal wall in (a) section A and (b) section B.

$$R_s = \sum_m \frac{R_{sm}}{\mu_0} \frac{\partial L}{\partial n_m} \quad (3.3)$$

where $\partial L / \partial n_m$ denotes the derivative of L with respect to incremental recession of wall m , in the normal direction to this wall, and R_{sm} is the surface resistance of the wall m .

The attenuation constant due to the conductor loss is defined as

$$\begin{aligned} \alpha_c &= \frac{\text{Power loss in conductors}}{2 \times \text{Power transmitted}} = \frac{P_c}{2P} \\ &= \frac{|I|^2 R}{2 |I|^2 Z_c} = \frac{1}{2 \mu_0 Z_c} \sum_m R_{sm} \frac{\partial L}{\partial n_m} \end{aligned} \quad (3.4)$$

where Z_c is the characteristic impedance of the transmission line under the assumption of negligible loss and I is the total current on each conductor. The inductance L is then expressed in terms of the characteristic impedance of the transmission line with the dielectric material replaced by air, Z_c^a :

$$L = \frac{Z_c^a}{\sqrt{\mu_0 \epsilon_0}} \quad (3.5)$$

After L in Eq. (3.5) is replaced by the above expression, the attenuation constant can be expressed in terms of the characteristic impedance Z_c^a :

$$\alpha_c = \sqrt{\frac{\epsilon_0}{\mu_0}} \frac{1}{2 Z_c} \sum_m R_{sm} \frac{\partial Z_c^a}{\partial n_m} \quad (3.6)$$

The characteristic impedance, Z_c , can be obtained from section 2.5. For Z_c^a , the quasi-static formula in [17] is used. That is, for section A:

$$Z_c^a = \frac{60\pi}{\frac{K(k_1)}{K(k_1')} + \frac{K(k_2)}{K(k_2')}} \quad (3.7)$$

where

$$k_1 = \frac{s}{s+2w} \quad (3.8)$$

$$k_2 = \frac{\tanh(\frac{\pi s}{4b})}{\tanh(\frac{\pi(s+2w)}{4b})} \quad (3.9)$$

$$k_1' = \sqrt{1 - k_1^2} \quad (3.10)$$

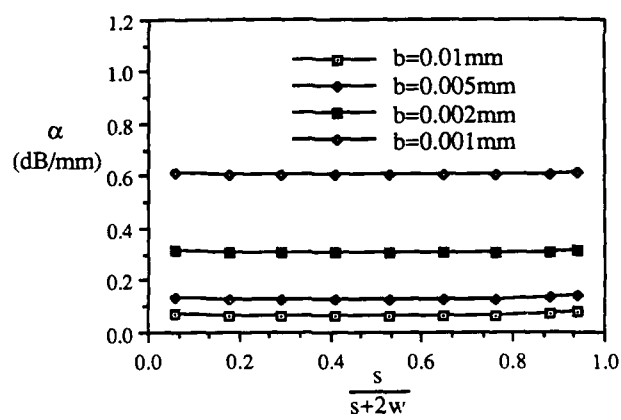
$$k_2' = \sqrt{1 - k_2^2} \quad (3.11)$$

and $K(k)$ is the complete elliptic integral of the first kind.

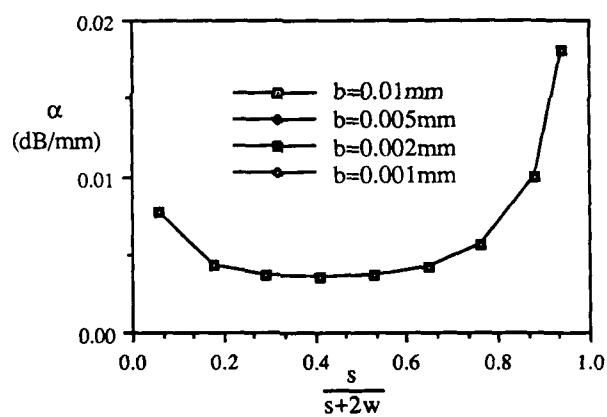
For section B:

$$Z_c^a = \frac{30\pi}{\frac{K(k_1)}{K(k_1')}} \quad (3.12)$$

From Eq.(3.6), Eq. (3.7), and Eq. (3.12), we can obtain the conductor loss of the transmission lines.



(a)



(b)

Fig. 3.2 The conductor loss of the constituent sections: (a) section A and (b) section B.

The attenuation constants of section A's and section B's with the circuit parameters varied are shown in Fig.3.2 (a) and Fig 3.2(b), respectively. The materials and physical sizes used are the same as those of Fig. 2.8, except otherwise noted. The conductor in these figures is Au, with thickness of $1.5\mu\text{m}$. As shown in these figures, the conductor loss of section A, which dominates the loss of the periodic structure, becomes larger with thinner dielectric overlay. Therefore, we need to find a modified structure to reduce the loss and to retain the slow-wave factor at the same time.

3.2 The Modified Structure

Since the crosstie-overlay slow-wave structure is too lossy to be used as a practical circuit element, the structure is modified to reduce the conductor loss. From the discussion in section 3.1, the thickness of the dielectric overlay should be increased to reduce the conductor loss. Yet, this will reduce the slow-wave effect at the same time from the discussion in chapter 2. A close inspection of the slow-wave mechanism of the crosstie-overlay slow-wave structure reveals the remedy. From the discussion in chapter 2, the slow-wave effect in the structure comes from the periodic loading of low-impedance transmission line sections (section A's). Also expressed in Eq.(2.21), the slow-wave factor is proportional to the square root of the impedance ratio between section A and section B. Therefore, in order to increase the impedance ratio between these two sections, the uniform coplanar waveguide in the original structure is replaced with a zig-zag coplanar waveguide as shown in Fig.3.3. To decrease the impedance of section A, the center conductor of the coplanar waveguide in section A is changed to a

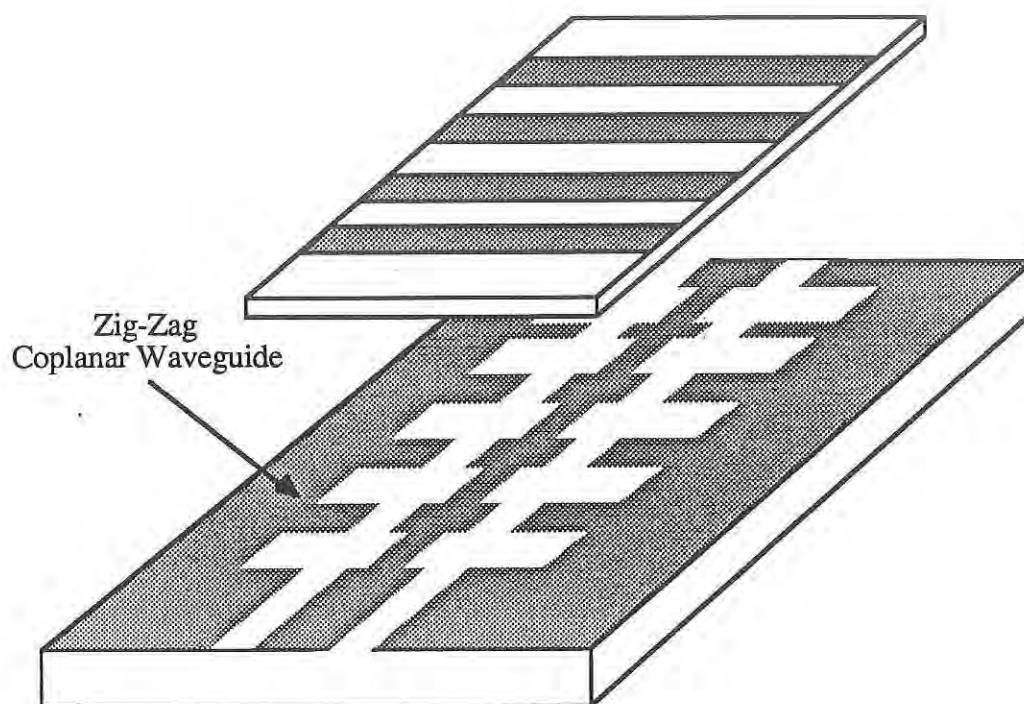


Fig. 3.3(b) The anatomical view of the modified crosstie slow-wave structure. The dielectric is removed from the substrate for clearer presentation.

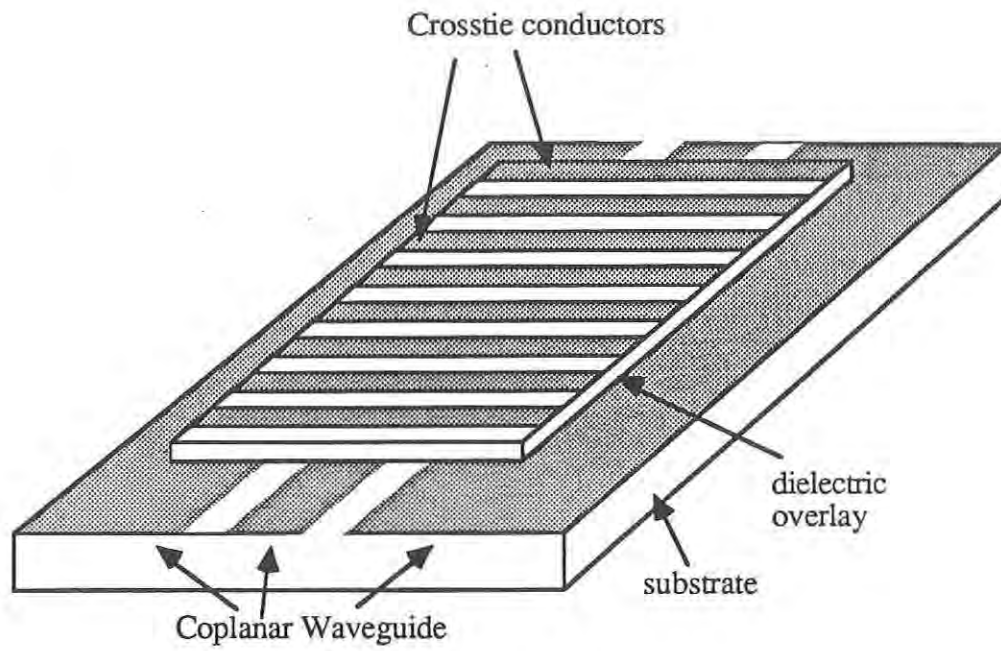


Fig. 3.3(a) The perspective view of the modified structure.

wider strip and the gap between the center strip and the ground plane is replaced with a thinner gap. The reverse is done for section B to increase the impedance.

To demonstrate the slow-wave propagation in the modified crosstie-overlay structure, a circuit as shown in Fig. 3.3 is fabricated. The calculated and measured slow-wave factors are shown in Fig. 3.4. The conductor loss of an original structure of equal slow-wave factor is shown in Table 3.1. To obtain the same slow-wave effect, the original structure is about five times as lossy as the modified structure. To demonstrate the slow-wave effect of the modified structure, the slow-wave factors of a uniform coplanar waveguide transmission line, a periodic coplanar waveguide, the original and modified crosstie-overlay slow-wave structure are compared in Table 3.2.

For the design data, the slow-wave factor and conductor loss of a modified structure with GaAs as substrate and Si_3N_4 as dielectric overlay are shown in Fig. 3.5. A comparison of the quality factors, Q 's, of the modified and the original crosstie-overlay slow-wave structure is shown in Fig. 3.6.

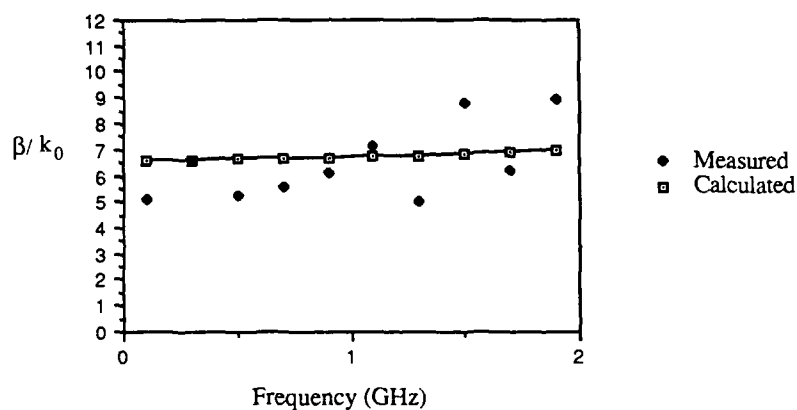


Fig. 3.4 Slow-wave factors versus frequency of the modified crosstie overlay slow-wave structure. Dielectric of dielectric overlay: 2.1. Dielectric of substrate: 2.55. Section A: $s=3.0\text{mm}$, $w=0.2\text{mm}$, $l=2\text{mm}$. Section B: $s=0.2\text{mm}$, $w=1.6\text{mm}$, $l=2\text{mm}$.

	β/k_0	α (dB/mm)
Modified Structure	7.00	0.0223
Original Structure	6.97	0.13

Table 3.1 Comparison of the crosstie overlay structures. The materials are as those used in Fig. 3.4. For the original structure, $s = 1.2\text{ mm}$, $w = 0.355\text{ mm}$, $t = 0.006\text{ mm}$.

	β/k_0
Section A	1.45
Section B	1.30
Periodic CPW	1.53
Periodic crosstie	2.92
Periodic CPW + Periodic crosstie	7.90

Table 3.2 Comparison of the slow-wave factors of different structures.

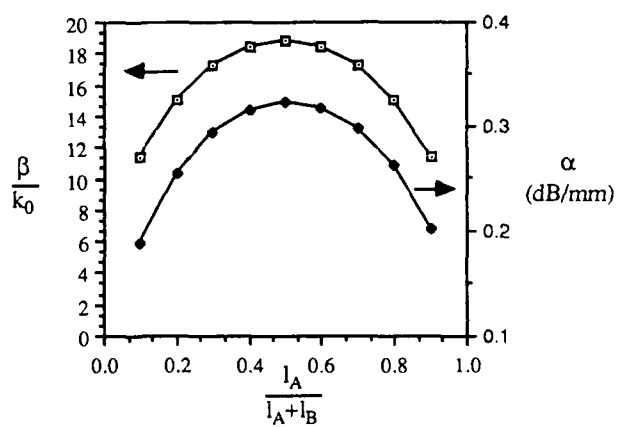


Fig. 3.5 The slow-wave factor and attenuation constant versus duty cycle of the modified cross-tie-overlay slow-wave structure. $f=10\text{GHz}$. $b=0.01\text{mm}$. Section A: $s=3.0\text{mm}$, $w=0.2\text{mm}$. Section B: $s=0.2\text{mm}$, $w=1.6\text{mm}$. All the other physical parameters are as those of Fig. 2.11.

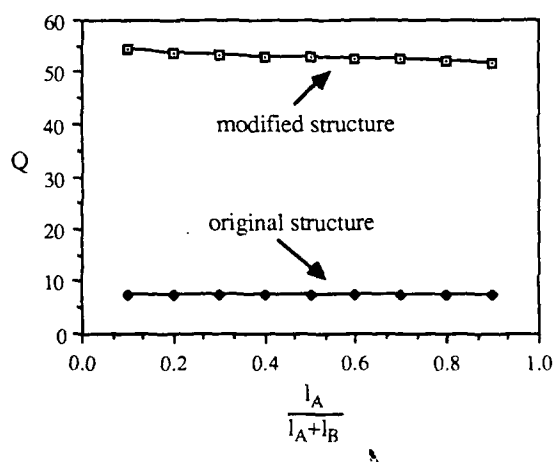


Fig. 3.6 Comparison of the quality factors of the modified and original crosstie-overlay slow-wave structure. The physical parameters for the modified structure is as those of Fig. 3.5. The physical parameters for the original are the same except: $b=0.001\text{mm}$, $s=2.6\text{mm}$, $w=0.4\text{mm}$.

CHAPTER 4: CIRCUIT APPLICATIONS

4.1 Introduction

After the propagation characteristics of the crosstie-overlay slow-wave structures have been studied in chapter 2 and chapter 3, two circuit applications of the structure will be presented in this chapter: (1) the design of a distributed Chebyshev bandstop filter, which will be introduced in section 4.2, and (2) the leaky-wave periodic antenna, which will be elaborated in section 4.3. The crosstie-overlay slow-wave structures are used as transmission lines in these circuits to reduce the circuit sizes.

4.2.1 Circuit Application I: Slow-wave Chebyshev Bandstop Filter

The design procedure of slow-wave Chebyshev bandstop filters begins with designing an appropriate transmission-line prototype circuit which uses equal electrical length transmission line sections as shown in Fig. 4.1. This prototype distributed filter consists of n slow-wave transmission-line sections; each section is one quarter wavelength at the stopband center frequency with the characteristic impedances chosen to produce desired filter response. The following procedure for the prototype circuit is based on the synthesis procedure for a Chebyshev bandstop filter developed in [18], which in turn is a modified procedure for the step-impedance transformer developed in [19].

Let us assume that Fig. 4.2 is the attenuation response of the circuit in Fig. 4.1. This idealized attenuation response can be defined in terms of Chebyshev

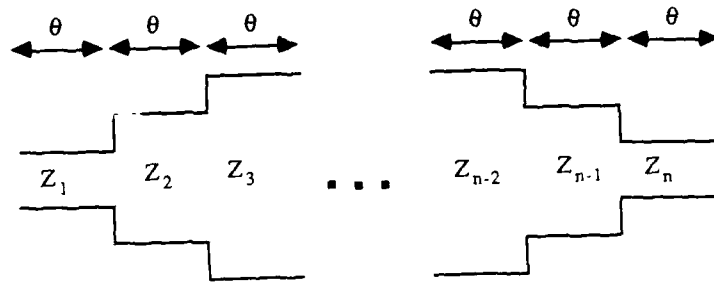


Fig. 4.1. Distributed Chebyshev bandstop filter.

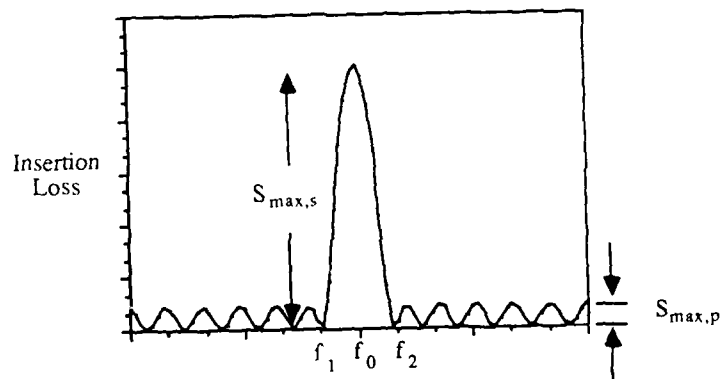


Fig. 4.2. The insertion loss of Chebyshev bandstop filter.

polynomials of degree n , the bandwidth, and the maximum stopband VSWR $S_{\max,s}$.

The insertion loss (IL) of an n -section Chebyshev bandstop filter, is

$$IL = 10 \log_{10} \left[1 + \frac{(S_{\max,s} - 1)^2 T_n^2 \left(\frac{\sin \theta}{\sin \theta_1} \right)}{4 S_{\max,s} T_n^2 \left(\frac{1}{\sin \theta_1} \right)} \right] \quad (\text{dB}) \quad (4.1)$$

where $T_n(x)$ is the Chebyshev polynomial of degree n . $S_{\max,s}$ is the maximum stopband VSWR. θ_1 is the electrical length of each section at the lower stopband edge frequency f_1 defined in Fig.4.2, and

$$\theta_1 = \frac{\pi}{2} \cdot \frac{f_1}{f_0} \quad (4.2)$$

$S_{\max,s}$ can be defined as the product of the junction VSWR's

$$S_{\max,s} = V_1 V_2 \cdots V_{n+1} \quad (4.3)$$

where V_i is the junction VSWR of the i th junction given by

$$V_i = \left(\frac{Z_i}{Z_{i-1}} \right)^{\pm 1} > 1. \quad (4.4)$$

Here, an appropriate sign should to be chosen in order to have V_i greater than one since the values of Z_i alternate up and down.

The sections required, n , can be determined in the following fashion once θ_1 (the fractional bandwidth), $S_{\max,s}$ (the maximum stopband VSWR), and $S_{\max,p}$ (the maximum passband VSWR) are given. From Eq.(4.1), evaluation of the insertion loss at $\theta=\theta_1$ gives

$$IL|_{\theta=\theta_1} = 10 \log_{10} \left[1 + \frac{(S_{\max,s} - 1)^2}{4S_{\max,s}} \frac{1}{T_n^2 \left(\frac{1}{\sin \theta_1} \right)} \right] \quad (4.7a)$$

$$= 10 \log_{10} \frac{1}{1 - |\rho_{\max,p}|^2} \quad (4.7b)$$

where $|\rho_{\max,p}|$ is the magnitude of the maximum passband reflection coefficient and is given by

$$|\rho_{\max,p}| = \frac{S_{\max,p} - 1}{S_{\max,p} + 1} \quad (4.8)$$

Equation (4.7b) can also be written in a form similar to (4.7a), that is,

$$IL|_{\theta=\theta_1} = 10 \log_{10} \left(1 + \frac{|\rho_{\max,p}|^2}{1 - |\rho_{\max,p}|^2} \right) \quad (4.9)$$

From (4.7a) and (4.9), the sections required can be expressed as:

$$n = \frac{\cosh^{-1} S}{\cosh^{-1} \left(\frac{1}{\sin \theta_1} \right)} \quad (4.10)$$

where

$$S = \frac{S_{\max, s} - 1}{2\sqrt{S_{\max, s}}} \sqrt{\left(\frac{S_{\max, p} + 1}{S_{\max, p} - 1} \right)^2 - 1} \quad (4.11)$$

After the required n is calculated by (4.11) for given specifications, we need to calculate the junction VSWR's V_i or the normalized section impedances Z_i . For the purpose of an approximate synthesis, as done in [20] for the case of a step-transformer, we assume that impedance steps are so small that the reflection interaction between steps can be neglected in the prototype circuit in Fig.4.1. Then the total reflection coefficient of the reflector prototype referred to at the center of the reflector structure is expressed as follows:

$$\rho = A_1 e^{jn\theta} - A_2 e^{j(n-2)\theta} + \dots + (-1)^n A_{n+1} e^{-jn\theta} \quad (4.12)$$

where the A_i 's are the junction reflection coefficient magnitudes, which are given by

$$A_i = \pm \frac{Z_i - Z_{i-1}}{Z_i + Z_{i-1}} > 0, \quad \text{for } i=1, 2, \dots, n+1. \quad (4.13)$$

The magnitude of the step reflections are assumed to be symmetrical, i.e., $A_1 = A_{n+1}$, $A_2 = A_n$, etc.. Therefore, for n odd

$$\rho = j \sum_{k=0}^{(n-1)/2} \left[(-1)^k 2A_{k+1} \sin(n-2k)\theta \right] \quad (4.14)$$

and for n even

$$\rho = \begin{cases} A_1, & \text{when } n=0 \\ \sum_{k=0}^{(n-2)/2} (-1)^k 2A_{k+1} \cos(n-2k)\theta + (-1)^{n/2} A_{\frac{n+2}{2}}, & \text{when } n \geq 2. \end{cases} \quad (4.15)$$

In order to obtain Chebyshev passbands, ρ in (4.14) or (4.15) is set to be equal to a Chebyshev polynomial $\alpha T_n(x)$, where α is a constant which need not be explicitly evaluated and

$$x = \frac{\sin \theta}{\sin \theta_1} \quad (4.16)$$

Following the evaluation procedure for A_i 's outlined in [18], we are able to determine the junction reflection coefficient magnitude ratios:

$$A_1 : A_2 : \dots : A_{n+1} = a_1 : a_2 : \dots : a_{n+1} \quad (4.17)$$

where $a_i = A_i/A_1$. Assuming the impedance steps are small, (4.13) can be written approximately as

$$A_i \approx \pm \frac{1}{2} \ln \frac{Z_i}{Z_{i-1}} > 0. \quad (4.18)$$

Substituting (4.18) into (4.17) and the impedance ratios can be obtained by:

$$\left| \ln \frac{Z_i}{Z_{i-1}} \right| = \begin{cases} \frac{a_i \left(\ln \frac{Z_1}{Z_0} + \ln \frac{Z_1}{Z_2} + \dots + \ln \frac{Z_n}{Z_{n+1}} \right)}{a_1 + a_2 + \dots + a_{n+1}}, & \text{for } n \text{ odd} \\ \frac{a_i \left(\ln \frac{Z_1}{Z_0} + \ln \frac{Z_1}{Z_2} + \dots + \ln \frac{Z_{n+1}}{Z_n} \right)}{a_1 + a_2 + \dots + a_{n+1}}, & \text{for } n \text{ even} \end{cases}$$

Neglecting the higher order reflections in each impedance step as well as using the approximation in (4.18) can introduce some errors in the above design procedure to obtain the Z_i/Z_{i-1} ratios. These errors include the bandwidth and the passband ripple size discrepancy. In order to reduce such errors, the above design procedure should be modified. From (4.1), it can be shown that the input reflection coefficient for an exact Chebyshev bandstop reflector design is

$$\rho_e = \frac{\frac{S_{\max,s}-1}{2\sqrt{S_{\max,s}}} T_n\left(\frac{\sin\theta}{\sin\theta_1}\right)}{\sqrt{1 + \frac{(S_{\max,s}-1)^2 T_n^2\left(\frac{\sin\theta}{\sin\theta_1}\right)}{4S_{\max,s} T_n^2\left(\frac{1}{\sin\theta_1}\right)}}} \quad (4.20)$$

The corresponding approximate equation which is consistent with ignoring higher order reflections is

$$\rho_a = \frac{1}{2} \ln(S_{\max,s}) \frac{T_n\left(\frac{\sin\theta}{\sin\theta_1}\right)}{T_n\left(\frac{1}{\sin\theta_1}\right)} \quad (4.21)$$

A correction was introduced by making the ripple sizes of (4.20) and (4.21) the same at the band edge. By replacing θ_1 with θ_1' in (4.21) and setting $\rho_a|_{\theta=\theta_1'} = \rho_e|_{\theta=\theta_1}$, we get

$$\theta_1' = \sin^{-1} \left[\frac{1}{\cosh \left(\frac{\cosh^{-1} S'}{\cosh^{-1} S} \cosh^{-1} \left(\frac{1}{\sin \theta_1} \right) \right)} \right] \quad (4.22)$$

where S is given in (4.11), θ_1 is given in (4.2), and

$$S' = \frac{\ln(S_{\max,s})}{S_{\max,p} - 1}. \quad (4.23)$$

Parameter θ_1' calculated using (4.22) is then used in place of θ_1 in (4.16) to generate all the junction reflection coefficients.

To determine the length of each line section, we require that each section is equal to quarter wavelength at the stopband center frequency, f_0 , or expressed as:

$$\beta_i L_i \Big|_{f=f_0} = \frac{\pi}{2} \quad \text{radians,} \quad i=1,2,\dots,n \quad (4.24)$$

where β_i is the propagation constant of section i at frequency f_0 .

In summary, in the design procedure stated above, the following specifications are given to obtain a Chebyshev response:

- (1) The stopband maximum VSWR, $S_{\max,s}$.
- (2) The passband maximum VSWR, $S_{\max,p}$.
- (3) The stopband fractional bandwidth.
- (4) The stopband center frequency.

The following desired design parameters are obtained from the above specifications:

- (1) Sections of quarter-wavelength transmission lines needed.
- (2) Impedance ratios.
- (3) Load impedances (assumed to be 1 Ohms in the prototype circuit).
- (4) Lengths of the quarter-wavelength transmission lines.

4.2.2 Circuit Example

In this section, a Chebychev bandstop filter suitable for the MMIC is designed by the procedure outlined in section 4.2.1 with the following circuit specifications :

- (1) Stopband center frequency: 5 GHz.
- (2) Fractional bandwidth: 0.25.
- (3) Stopband maximum attenuation: 10 dB
- (4) Passband maximum attenuation: 0.5 dB.

After the synthesis outlined in section 4.2.1 is carried out, 15 sections are needed for the bandstop filter. And the impedances required for each section are, with the input impedance equal to 13 Ω :

$Z_1=21.90 \Omega$, $Z_2=18.91 \Omega$, $Z_3=22.27 \Omega$, $Z_4=18.63 \Omega$, $Z_5=22.55 \Omega$, $Z_6=18.45 \Omega$,
 $Z_7=22.70 \Omega$, $Z_8=18.39 \Omega$.

The filter is a symmetrical structure. Therefore, the rest of the impedance sections need not to be reiterated.

A 3-section impedance transformer is also designed to transform the input impedance from $13\ \Omega$ to $50\ \Omega$ used in most measuring systems. The impedances of these transformer sections are: $17.88\ \Omega$, $25.49\ \Omega$, and $36.36\ \Omega$.

The frequency response of the designed bandstop filter is shown in Fig. 4.3. Here, the substrate used is GaAs with thickness of 20 mils and the dielectric overlay is Si_3N_4 with thickness of 1 mil. The propagation constant and the characteristic impedance are calculated by the method developed in chapter 2. The conductor loss, calculated by the method developed in chapter 3, is also included in the circuit design. Since the synthesis procedure is for lossless case only, an estimate of the insertion loss shift is necessary for accurate circuit design. The formula developed in [21] is used to estimate the insertion loss at passband. At $f = 10\text{GHz}$, the estimated insertion loss is 2.4dB and the simulated loss in Fig.4.3(a) is 2.7dB.

For comparison, the same specifications are used for a bandstop filter with the original crosstie overlay slow-wave structure. The circuit performance is as shown in Fig.4.3(b). As shown in these figures, the modified structure reduces the conductor loss and makes the circuit useful.

4.3 Frequency Scanning Antenna

4.3.1 Design

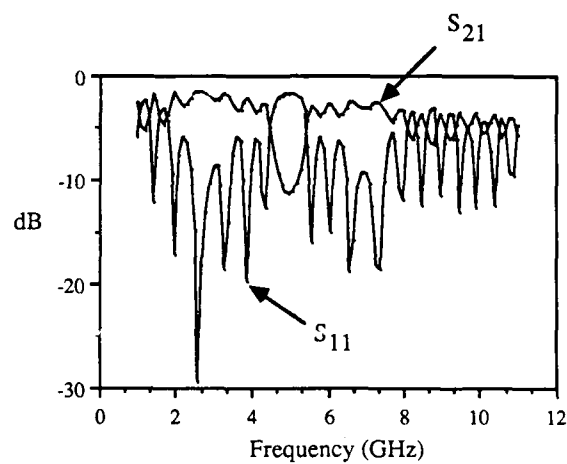


Fig. 4.3(a) The insertion loss and return loss of the bandstop filter with the modified cross-tie-overlay slow-wave structure. Section A: $s=3.0\text{mm}$, $w=0.2\text{mm}$. Section B: $s=0.1\text{mm}$, $w=1.65\text{mm}$. All the other physical parameters are as those of Fig. 2.11.

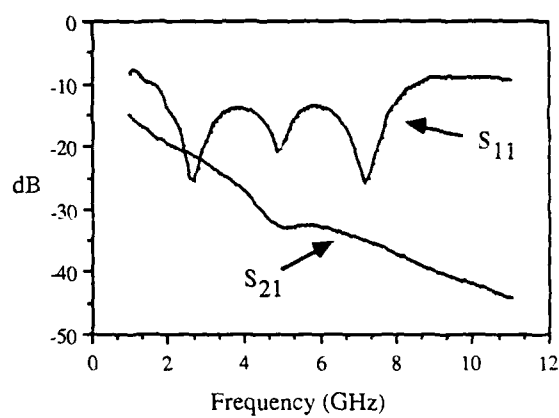


Fig. 4.3(b) The insertion loss and return loss of the band stop filter with the original cross-tie-overlay slow-wave structure. $s=0.15\text{mm}$, $w=0.745\text{mm}$, $b=0.001\text{m}$. All the other parameters are the same as Fig. 4.3(a)

Travelling-wave antenna arrays with frequency-scanning feature based on microstrip line have been shown to be successful [22], [23]. The basic idea of these designs is to perturb the uniform transmission line at equal distances (usually one guided-wavelength) to create the radiation source. Therefore, the feed and the radiation antenna are integrated in the same circuit.

In this circuit, the transmission lines in the travelling-wave antenna are replaced with crosstie-overlay slow-wave transmission lines to reduce the circuit size since the frequency-scanning arrays usually require a long transmission line. This antenna also has the feature that small change in frequency can steer the main beam widely.

The antenna is as shown in Fig.4.4 and the picture of the dissembled antenna in Fig. 4.5. This antenna is a doubly periodic structure. A periodic zig-zag coplanar waveguide couples the energy into the radiating resonators. To create slow-wave transmission lines, a layer of dielectric overlay and crosstie conductors are placed on top of the periodic coplanar waveguide. The leaky-wave stopband and the slow-wave propagation of periodic structures are utilized for radiation and for slow-wave transmission lines respectively. The length of a period of the crosstie-conductor is made to be much smaller than the guided wavelength to make it fall into the operating range of dispersionless transmission line. The period of the periodic antenna are made one guided wavelength at the desired broadside-radiating frequency. This frequency falls into the leaky-wave stopband region, or point B in the k - β diagram as shown in Fig. 1.4. The main beam direction of a leaky-wave antenna is as shown in Fig. 4.6:

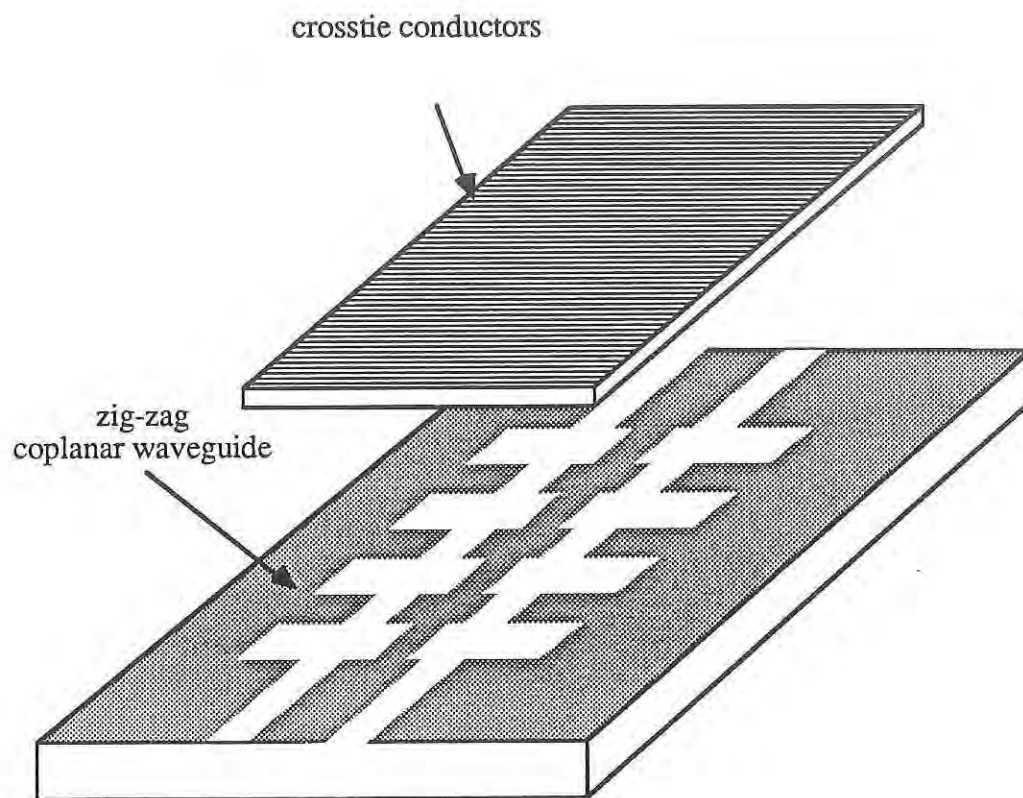


Fig. 4.4 The anatomical view of the frequency-scanning antenna. This structure is a doubly-periodic structure. The zig-zag coplanar waveguide is the bigger period and the smaller cross-tie conductor periodic structure provides the slow-wave transmission.

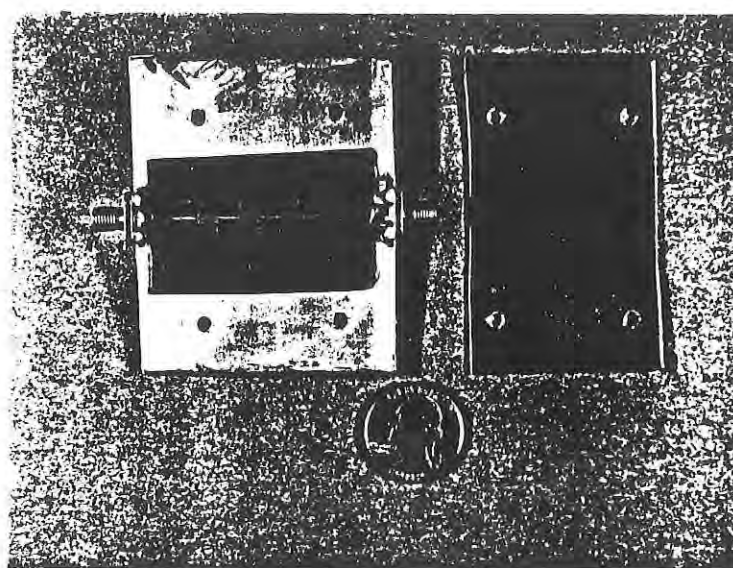


Fig. 4.5 The picture of the antenna circuit.

$$\sin\theta = \frac{\beta}{k_0} - \frac{2\pi}{k_0 d} \quad (4.25)$$

Although it is usually avoided in the circuit design, it is used here to steer the main beam for demonstration of the frequency-scanning. The antenna are tapered as in [24] to obtain better sidelobe performance.

For the slow-wave transmission lines, the dispersion relationship in section 2.3 for the periodic transmission lines is used to calculate the propagation constant of each section. After the propagation constant of each section is obtained, each resonant elements is made to be half wavelength at the desired frequency.

4.2.2 Measurement

The coplanar waveguide and crosstie conductors are fabricated on a woven PTFE substrate with thickness of 30 mils and dielectric constant of 2.55. Five radiation resonators are used. The total length of the antenna circuit is 45.8mm. The dielectric overlay used is Cufion with the thickness of 1 mil and dielectric constant of 2.1. The antenna is designed to radiate into the broadside direction (normal to the antenna array) at 6.22 GHz. The actual measured frequency is 6.77 GHz. The calculated and measured radiation pattern for this case is shown in Fig. 4.7. To demonstrate the slow-wave propagation, the insertion loss and return loss of the antenna circuit without and with the crosstie-conductors and dielectric overlay are shown respectively in Fig. 4.8(a) and Fig. 4.8(b). We can see from these figures that the first stopband has shifted to lower frequency in Fig. 4.8(b) with the crosstie-overlay attached. The antenna without the crosstie-conductors and dielectric overlay radiates into the broadside direction at 19.9 GHz. This shows that the crosstie-overlay

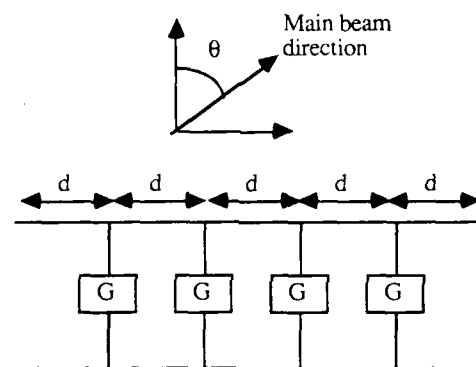


Fig. 4.6 Main beam direction of a leaky-wave antenna.

has the effect of reducing the size of the circuit three times. The frequency scanning feature of this antenna is also examined by changing the frequency. The results are listed in Table I.

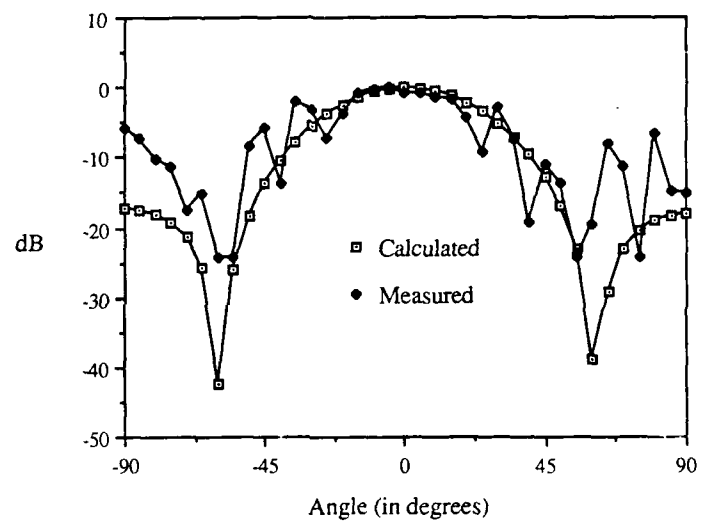


Fig. 4.7 The E-plane radiation pattern for the broadside radiation.

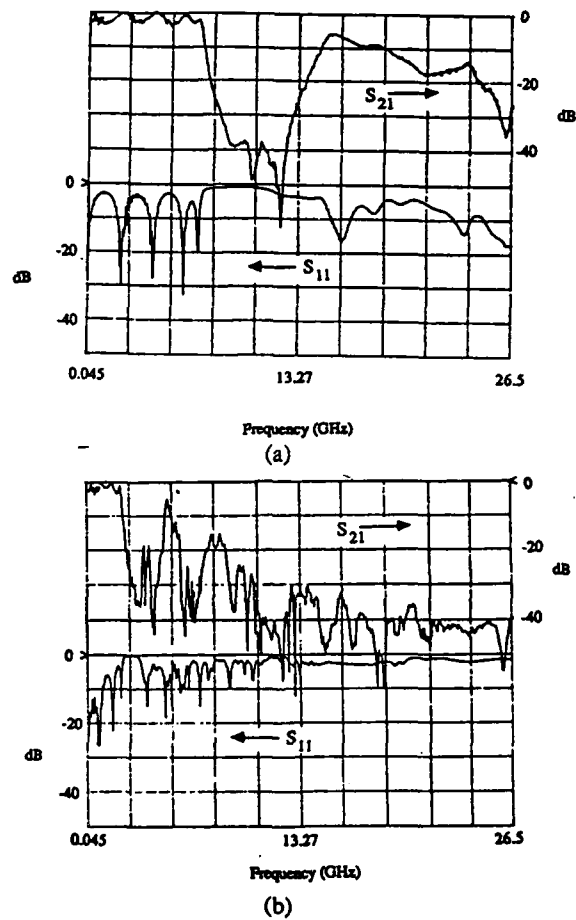


Fig. 4.8 The frequency response of the antenna circuit: (a) without and (b) with cross-tie conductors and dielectric overlay.

Freq. (GHz)	Calculated	Measured
6.4	-12.5 °	-10.0 °
6.6	-5.0 °	-5.0 °
7.0	5.0 °	5.0 °
7.2	12.5 °	11.0 °
7.4	17.5 °	15.0 °

Table 4.1 Comparison of the measured and the calculated direction of the main beam versus frequency.

CHAPTER 5: CONCLUSIONS

In this dissertation, we have presented the analysis and applications of the crosstie-overlay slow-wave structure. The slow-wave propagation in this structure is predicted by analysis and confirmed by experiments. The slow-wave property makes the crosstie-overlay structure a very suitable passive circuit element for monolithic microwave integrated circuits. In the modified structure, the conductor loss is reduced to make the crosstie-overlay structure a practical circuit element. The circuit applications, namely, the slow-wave Chebychev bandstop filters and the frequency scanning antenna, demonstrate the slow-wave property of the structure. These prototype design can be generalized according to the required specifications.

There are several applications worthy of further investigation that are extensions of the applications mentioned above. For example, two paralleled coupled bandstop filters can produce a bandpass filter, as mentioned in [25]. Also, the radiation elements in the frequency scanning antenna can be replaced with the slot dipole antenna as in [26]. These antenna arrays have the feature of high VSWR; therefore, they can serve as reflector of an oscillator and the radiation element of the antenna at the same time. This approach of circuit application can integrate the source and the radiation element into one circuit as shown in [24].

APPENDIX I: SPECTRAL DOMAIN GREEN'S FUNCTION

$$\hat{Y}_{xx}^{11} = Y_v^{11} \sin^2\theta + Y_u^{11} \cos^2\theta \quad (\text{A.I.1})$$

$$\hat{Y}_{xz}^{11} = \hat{Y}_{zx}^{11} = (Y_v^{11} - Y_u^{11}) \sin\theta \cos\theta \quad (\text{A.I.2})$$

$$\hat{Y}_{zz}^{11} = Y_u^{11} \sin^2\theta + Y_v^{11} \cos^2\theta \quad (\text{A.I.3})$$

$$\hat{Y}_{xx}^{12} = Y_v^{12} \sin^2\theta + Y_u^{12} \cos^2\theta \quad (\text{A.I.4})$$

$$\hat{Y}_{xz}^{12} = \hat{Y}_{zx}^{12} = (Y_v^{12} - Y_u^{12}) \sin\theta \cos\theta \quad (\text{A.I.5})$$

$$\hat{Y}_{zz}^{12} = Y_u^{12} \sin^2\theta + Y_v^{12} \cos^2\theta \quad (\text{A.I.6})$$

$$\hat{Y}_{xx}^{21} = Y_v^{21} \sin^2\theta + Y_u^{21} \cos^2\theta \quad (\text{A.I.7})$$

$$\hat{Y}_{xz}^{21} = \hat{Y}_{zx}^{21} = (Y_v^{21} - Y_u^{21}) \sin\theta \cos\theta \quad (\text{A.I.8})$$

$$\hat{Y}_{zz}^{21} = Y_u^{21} \sin^2\theta + Y_v^{21} \cos^2\theta \quad (\text{A.I.9})$$

$$\hat{Y}_{xx}^{22} = Y_u^{22} \sin^2\theta + Y_v^{22} \cos^2\theta \quad (\text{A.I.10})$$

$$\hat{Y}_{xz}^{22} = \hat{Y}_{zx}^{22} = (Y_v^{22} - Y_u^{22}) \sin\theta \cos\theta \quad (\text{A.I.11})$$

$$\hat{Y}_{zz}^{22} = Y_u^{22} \sin^2 \theta + Y_v^{22} \cos^2 \theta \quad (\text{A.I.12})$$

where

$$Y_v^{11} = Y_{TM4} + Y_{TM3} \coth(\gamma_3 b) \quad (\text{A.I.13})$$

$$Y_u^{11} = Y_{TE4} + Y_{TE3} \coth(\gamma_3 b) \quad (\text{A.I.14})$$

$$Y_v^{12} = Y_v^{21} = -Y_{TM3} \sinh(\gamma_3 b) \quad (\text{A.I.15})$$

$$Y_u^{12} = Y_u^{21} = -Y_{TE3} \sinh(\gamma_3 b) \quad (\text{A.I.16})$$

$$Y_v^{22} = \frac{Y_{TM2}(Y_{TM1} + Y_{TM2} \tanh(\gamma_2 h))}{Y_{TM2} + Y_{TM1} \tanh(\gamma_2 h)} + Y_{TM3} \coth(\gamma_3 b) \quad (\text{A.I.17})$$

$$Y_u^{22} = \frac{Y_{TE2}(Y_{TE1} + Y_{TE2} \tanh(\gamma_2 h))}{Y_{TE2} + Y_{TE1} \tanh(\gamma_2 h)} + Y_{TE3} \coth(\gamma_3 b) \quad (\text{A.I.18})$$

APPENDIX II: BASIS FUNCTIONS

1. Maxwell functions:

$$M_n^1(x) = \frac{\cos(\frac{n\pi x}{w})}{\sqrt{(\frac{w}{2})^2 - x^2}} \quad \frac{w}{2} \leq x \leq \frac{w}{2} \quad (\text{A.II.1})$$

$$M_n^2(x) = \frac{\sin(\frac{n\pi x}{w})}{\sqrt{(\frac{w}{2})^2 - x^2}} \quad \frac{w}{2} \leq x \leq \frac{w}{2} \quad (\text{A.II.2})$$

The Fourier transforms of these functions are:

$$F(M_n^1(x)) = \frac{\pi}{2} \left\{ J_0\left(\frac{n\pi}{2} + \frac{\alpha w}{2}\right) + J_0\left(\frac{n\pi}{2} - \frac{\alpha w}{2}\right) \right\} \quad (\text{A.II.3})$$

$$F(M_n^2(x)) = \frac{\pi}{2j} \left\{ J_0\left(\frac{n\pi}{2} + \frac{\alpha w}{2}\right) - J_0\left(\frac{n\pi}{2} - \frac{\alpha w}{2}\right) \right\} \quad (\text{A.II.4})$$

where $F(\cdot)$ denotes Fourier transform, α is the Fourier transform variable, and J_0 is first kind Bessel function of zeroth order.

2. Triangular function

$$\begin{aligned} \Lambda(x) &= 1 - \frac{x}{a} \quad 0 \leq x \leq a \\ &= 1 + \frac{x}{a} \quad -a \leq x \leq 0 \end{aligned} \quad (\text{A.II.5})$$

The Fourier transform of this function is:

$$F(\Lambda(x)) = a \operatorname{sinc}^2\left(\frac{a\alpha}{2}\right) \quad (\text{A.II.6})$$

3. Legendre polynomials:

$$P_n(x) = \frac{1}{2^n} \sum_{m=0}^{\left[\frac{n}{2}\right]} (-1)^m \binom{n}{m} \binom{2n-2m}{n} x^{n-2m} \quad -1 \leq x \leq 1 \quad (\text{A.II.7})$$

The Fourier transform of this function is:

$$F(P_n(x)) = 2 (j)^n J_n(\alpha) \quad (\text{A.II.8})$$

where J_n is the spherical Bessel function of n -th order.

BIBLIOGRAPHY

1. R. A. Pucel, "Design considerations for monolithic microwave circuits," *IEEE Trans. Microwave Theory Tech.*, vol.MTT-29, pp.513-534, 1981.
2. H. Hasegawa, M. Furukawa and H. Yanai, "Properties of microstrip line on Si-SiO₂ system," *IEEE Trans. Microwave Theory Tech.*, vol.MTT-19, pp.869-881, 1971.
3. Y. Fukoka, Y. C. Shih and T. Itoh, "Analysis of slow-wave coplanar waveguide for monolithic integrated circuits," *IEEE Trans. Microwave Theory Tech.*, vol.MTT-31, pp.567-573, 1983.
4. C. M. Krowne and R. E. Neidert, "Slow wave monolithic variable phase shifter," 10th Int. Conf. Infrared and Millimeter Waves, Lake Buena Vista, FL, Dec.9-13, 1985, pp.275-276.
5. P. Cheung, D. Fun, D. Miller, C. -K. C. Tzuang, D. P. Neikirk and T. Itoh, "Optically controlled coplanar waveguide millimeter wave phase shifter," 10th Int. Conf. Infrared and Millimeter Waves, Lake Buena Vista, FL, Dec.9-13, 1985, pp.303-304.
6. Y. D. Lin, D. P. Neikirk, and T. Itoh, "Coplanar waveguide phase shifter controlled by a spatially periodic optical illumination," *International Journal of Infrared and Millimeter Waves*, vol. 8, no. 9, 1987, pp.1027-1036.

7. S. Seki and H. Hasegawa, "Cross-tie slow-wave coplanar waveguide on semi-insulating GaAs substrates," *Electronics Letters*, vol.17, no.25, pp.940-941, Dec.10, 1981.
8. T. H. Wang and T. Itoh, "Compact grating structure for application to filters and resonators in monolithic microwave integrated circuits," *IEEE Trans. Microwave Theory Tech.*, vol. MTT-35, pp. 1176-1182, Dec. 1987.
9. H. Q. Tserng, H. M. Macksey and S.R. Nelson, "Design, fabrication, and characterization of monolithic microwave GaAs power FET amplifiers," *IEEE Trans. Electron Devices*, vol. ED-28, no. 2, Feb. 1981, pp.183-190.
10. R. E. Collin, *Foundations for microwave engineering* (New York: McGraw-Hill, 1972), pp. 381-383.
11. T. Itoh and R. Mittra, "Spectral-domain approach for calculating the dispersion characteristics of microstrip lines," *IEEE Trans. Microwave Theory Tech.*, vol.MTT-21, pp.496-499, 1973.
12. T. Itoh and R. Mittra, "Dispersion characteristics of slot lines," *Electronics Letters*, vol.7, no.13, pp.364-365, 1971.
13. T. Itoh, "Spectral domain immittance approach for dispersion characteristics of generalized printed transmission lines," *IEEE Trans. Microwave Theory Tech.*, vol.MTT-28, pp.733-736, 1980.

14. R. H. Jansen, "High-speed computation of single and coupled microstrip parameters including dispersion, high-order modes, loss and finite strip thickness," *IEEE Trans. Microwave Theory Tech.*, vol.MTT-26, pp.75-82, 1978.
15. R. H. Jansen, "Unified user oriented computation of shielded, covered and open planar microwave and millimeter-wave transmission line characteristics," *Microwaves, Opt. Acoust.*, vol.MOA-1, pp.14-22, January 1979.
16. H. A. Wheeler, "Formulas for the skin effect," *Proceedings of IRE*, vol.30, 1942, pp.412-424.
17. G. Ghione and C. U. Naldi, "Coplanar waveguides for MMIC applications: Effect of upper shielding, conductor backing, finite-extend ground planes, and line-to-line coupling," *IEEE Trans. Microwave Theory Tech.*, vol.MTT-35, pp.260-267, 1987.
18. D. C. Park, G. L. Matthaei and M. S. Wei, "Bandstop filter design using a dielectric waveguide grating," *IEEE Trans. Microwave Theory Tech.*, vol.MTT-33, pp.693-702, 1985.
19. S. B. Cohn, "Optimum design of stepped transmission-line transformers," *IRE IEEE Trans. Microwave Theory Tech.*, vol.MTT-3, pp.16-21, 1955.
20. R. E. Collin, "Theory and design of wide-band multisection quarter-wave transformers," *Proceedings of IRE*, vol.43, pp.179-185, 1955.

21. L. Young, "Prediction of absorption loss in multilayer interference filters," *Journal of the Optical Society of America*, vol. 52, no. 7, July 1962, pp. 753-761.
22. I. J. Bahl and P. Bhartia, *Microstrip Antennas*, pp. 212-213, Artech House, 1980.
23. M. Danielsen and K. Jorgensen, "Frequency scanning microstrip antennas," *IEEE Trans. Antennas Propagat.*, vol. AP-27, pp. 146-150, Mar. 1979.
24. J. Birkeland and T. Itoh, "FET-based planar circuits for quasi-optical sources and transceivers," *IEEE Trans. Microwave Theory Tech.*, vol. MTT-37, pp. 1452-1459, Sept. 1988.
25. G. L. Matthaei et al, "A study of the filter properties of single and parallel-coupled dielectric-waveguide gratings," *IEEE Trans. Microwave Theory Tech.*, vol. MTT-31, pp. 825-835, Oct. 1983.
26. A. Nesic, "Slotted antenna array excited by a coplanar waveguide," *Electron. Lett.*, vol. 18, no. 6, pp. 275-276, Mar. 1982.